Quantification of the predisposing role of tectonics and landscape evolution in the occurrence of massive rock failures: the Loumar landslide (Zagros Belt, Iran)

Michele Delchiaro[1], Marta Della Seta[1], and Salvatore Martino[1]

[1] Sapienza University of Rome, Department of Earth Sciences, Rome (Italy)

Corresponding author: Michele Delchiaro (michele.delchiaro@uniroma1.it)

Key Points:

- Reconstruction of Quaternary tectonic and landscape evolution of the Gavar fold (Zagros Mts., Iran) and the associated gravity-induced slope deformation.
- Fluvial linear inversion modelling of the drainage network of the fold allowed to identify the temporal step at which Mass Rock Creep (MRC) started to deform the slope, related to a meander abandonment in the ancient course of the Seymareh River, thus favouring the kinematic release of a large rock mass along the flank of the fold.
- OSL dating provided an age of 5.52±0.36 ka for pond sediments deposited upstream of the landslide due to the partial damming of the river.

Abstract

This research focuses on the Loumar deformation which affected the NE slope of the Gavar anticline (Zagros Mts., Iran). The landslide evolution is strictly related to the growth of the fold and to the evolution of the Seymareh river drainage system. In this regard, we infer the Quaternary tectonic and landscape evolution of the fold, as well as the chronology of the events that led to the deformation and following failure, through geomorphometric analyses, as well as field surveying and OSL dating of geomorphic markers. Assuming a block uplift model, the drainage network of Gavar fold recorded 1.3±0.1 Myr of tectonic history that describes the lateral propagation of the fold towards NW. According to the inversion history, the formation of a parasitic fold at 0.16 ± 0.015 Ma led to a meander abandonment in the ancient course of the Seymareh River, thus favoring the kinematic release of a large rock mass along the flank of the fold. The latter allowed the initiation of the deformation, which culminated in a huge rockslide at 5.52±0.36 ka, as constrained by the OSL age of sediments deposited upstream in a pond caused by the partial damming of the river. Finally, InSAR techniques were applied by processing 181 satellite Sentinel-1 radar images of the ascending and descending orbit, spanning from 16 May 2016 to 21 November 2019. It has been observed that the rockslide is still moving downslope with a maximum displacement rate of 7.5 mm y^{-1} in the trench zone.

Plain Language Summary

The Loumar landslide detached from the NE slope of the Gavar fold in the Zagros Mountains (Iran) covering an area of 3 km^2. The landslide evolution is strictly related to the fold growth and to the erosion of the Seymareh river drainage system. Specifically, it acted as a slow deformation for a long time by a viscous process (MRC), after which it accelerated and failed as a viscous rockslide. The failure partially dammed the river, generating a pond. In this regard, we reconstructed the tectonic evolution of the fold over 1.3±0.1 Myr quantitatively analyzing the river network, with a modelling method called linear inversion. We discover that at 0.16 ± 0.015 Ma the formation of a minor fold along the flank of the main structure led to a meander abandonment in the ancient course of the river, releasing a large rock mass and thus initiating the deformation. We dated the pond sediments at 5.52±0.36 ka with Optically Stimulated Luminescence (OSL) method, thus constraining the time for failure. Finally, we measured through satellite interpherometry technique that the rockslide is still moving downslope with a maximum displacement rate of 7.5 mm y^{-1}.

1 Introduction

The topography of tectonically active regions shows the dynamic feedback between tectonic and surface processes (Agliardi et al., 2009; Korup et al., 2010; Larsen & Montgomery, 2012; Montgomery & Brandon, 2002). Hillslopes adjust to high rates of rock uplift and erosion attaining a threshold angle characteristic of limit equilibrium conditions of slope failure (Larsen & Montgomery, 2012; Montgomery & Brandon, 2002; Roering et al., 2009). As hillslope angles approach the threshold angle, landslide erosion rates are predicted to increase nonlinearly until the latter is exceeded by gravitational stress and bedrock landslides occur (Korup et al., 2007; Larsen & Montgomery, 2012; Montgomery & Brandon, 2002). In addition to these types of landslides, in such active landscapes large-scale, gravity-induced slope deformations (Deep-Seated Gravitational Slope Deformations DSGSD Auct.) often occur. These processes are large mass movements involving high-relief slopes on which Mass Rock Creep (MRC; Chigira, 1992) acts on a large spatio-temporal scale through a continuous and non-linear variation of the stress-

strain state (Pànek & Klimeš, 2016; Petley & Allison, 1997; Saito, 1969). Field evidence of the deformation process are the tension features (such as scarps, trenches, tension cracks) in the upper slopes, the buckling folds that often occur in the middle part of the deforming rock mass, the bulging and other compressional features affecting the slope toe (Agliardi et al., 2009; Crosta et al., 2013; Discenza et al., 2011; Martino et al., 2004). In general, gravity-induced slope deformations appear closely linked to specific geological and structural features (bedding, folding, faulting, etc.) and topographic factors mainly due to the evolution of drainage networks (Agliardi et al., 2009, Crosta et al., 2013). Furthermore, it has been demonstrated in various works how the morpho-evolution of mountain slopes, correlated both to tectonic and erosive processes, can regulate the initiation and development of these processes (Bozzano et al., 2012, 2016; Della Seta et al., 2017; Martino et al., 2017). In a tectonically active region, the combined effects of tectonics, fluvial incision and hillslope processes generate high-relief, narrow river valleys and gorges (Boulton et al., 2014; Hiraishi & Chigira, 2011; Korup & Schlunegger, 2007; Lague, 2014; Tsou et al., 2014). In such a landscape, knickpoints migrating upward due to a base level drop mark a rejuvenation of the drainage system. They are defined as a fluvial portion of the transient boundary between adjusting and relict topography that links upward low relief areas to downstream segments, with increasing vertical drop (Clark et al., 2005; Crosby and Whipple, 2006; Harkins et al., 2007; Schmidt et al., 2015). The temporal and spatial characteristics of the perturbation determine the fluvial response to the forcing (faulting, tilting, folding) in terms of vertical and horizontal drop of the knickpoint (Boulton et al., 2014). A discrete event, such as a locally stiff bedrock, a debris flow or landslide, can cause a deviation away from equilibrium (Kirby & Whipple, 2012, Walsh et al., 2012), generating a 'vertical-step knickpoint' (Kirby & Whipple, 2012) that can be recognised on a slope-area plot as a spike in slope values. By contrast, 'slope-break knickpoints' (Kirby & Whipple, 2012) break the slope-area scaling and develop as a response to a persistent change in forcing that drives the fluvial system towards a new equilibrium (Tucker & Whipple, 2002). Such forcing mechanisms may be due to the initiation of faulting or to a change in slip rate along a fault and as such slope-break knickpoints enable the interpretation of tectonics in erosional landscapes (Kirby & Whipple, 2012, Wobus et al., 2006).

In this regard, the fluvial topography has the potential to record transient variations of tectonic uplift by solving the analytical solution of the linear transient stream power incision model (e.g., Goren et al., 2014) and over the past decade, the longitudinal profiles of rivers have been numerically inverted to decipher the history of uplift for several orogens all over the world (Fox et al., 2014; Goren et al., 2014; Ma et al., 2020; Pritchard et al., 2009; Roberts & White, 2010; Rudge et al., 2015).

The Loumar slope deformation is here presented as case study that evolved into a rockslide affecting the NE slope of the Gavar anticline in the Simply Folded Zagros. Its evolution could be strictly related to the vertical and lateral growth of the anticline and to the evolution of the Seymareh River drainage system whose erosional rejuvenation, due to the uplift forcing, could have kinematically released a rock mass, likely causing the initiation of the deformational process. It is located almost 90 km northwest of the Seymareh landslide, internationally recognized as the largest landslide on Earth's surface (Delchiaro et al. 2019, 2020a, and reference therein). The case study represents an impressive example in which tectonics and fluvial network evolution originated the predisposing conditions for Mass Rock Creep process development. Therefore, the main goal of this work is to define the Quaternary

tectonic and landscape evolution of the Gavar fold and in particular the chronology of the events that led to the gravitational deformation.

2 The Seymareh river basin in the Zagros Mountains

The Zagros Mountains extend for 2000 km from the Taurus Mountains in the northern Iraq and Turkey to the Makran accretionary prism, in the southeast of the Fars. The Zagros orogeny results from the collision of continental blocks of Arabia and Eurasia and the consequent consumption of the Neotethys Ocean due to the NE-dipping subduction beneath Iran since Late Cretaceous times (Golonka, 2004; McQuarrie, 2004; Mouthereau et al., 2012; Stampfli & Borel, 2002; Talbot & Alavi, 1996).

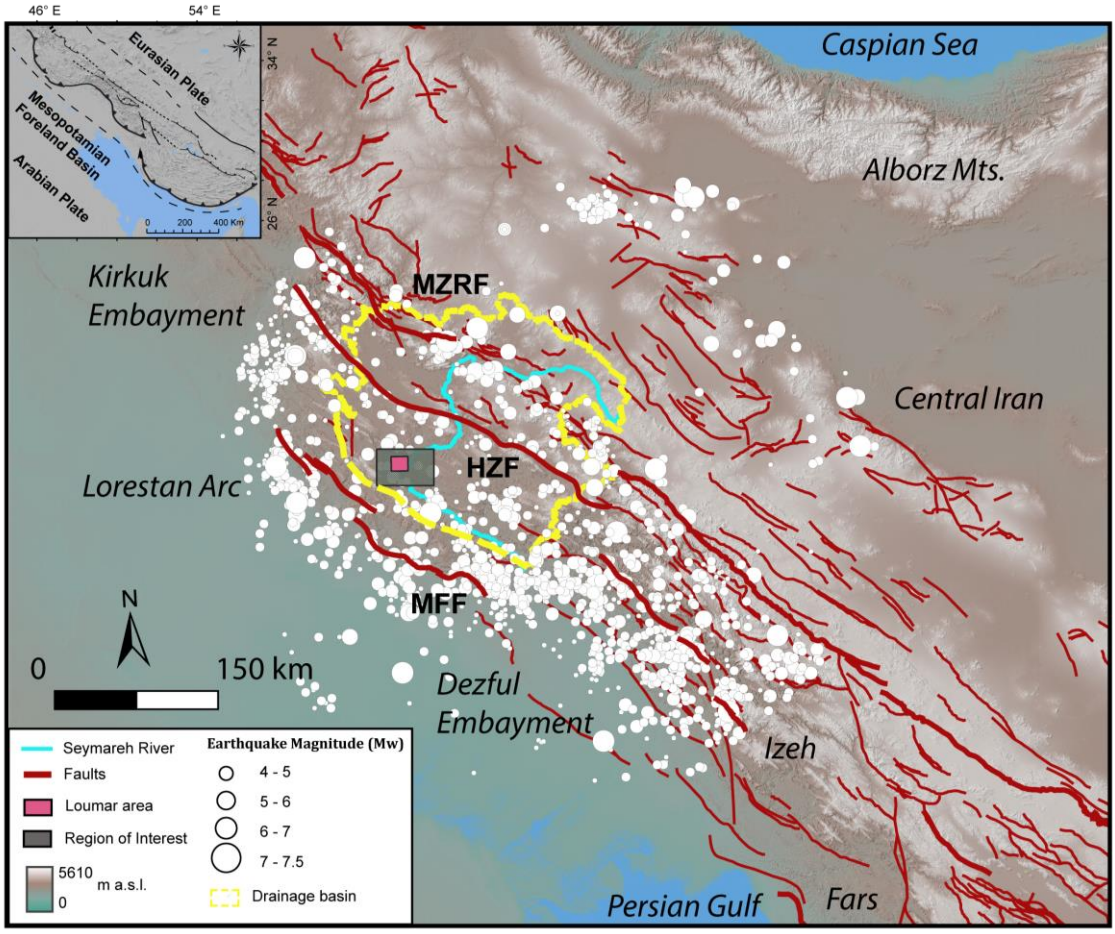

Figure 1. Regional sketch of the Zagros Mountains. MFF: Mountain Front Fault, HZF: High Zagros Fault, MZRF: Main Zagros Reverse Fault.

The Seymareh river basin (Figure 1) lies within the north-western part of the belt. With a total extent of at least 42,000 km^2, its drainage network dissects most of the Push-e Kuh Arc (Verges et al. 2011): from the hinterland of the chain it passes in the Lorestan region where it flows into the Karkheh River, a major tributary of the Tigris whose mouth is located in the Persian Gulf. The Seymareh River crosses several tectonic units of the mountain range, from NE to SW: Sanandaj-Sirjan Zone, the Imbricate Zone, the Zagros (Simply) Folded Belt and the continental Mesopotamian Foreland (Agard et al., 2005, and references therein). These are

bounded by regional-scale tectonic lineaments such as the Main Zagros Thrust (MZT), High Zagros Fault (HZF), and Mountain Front Fault (MFF). The growth of anticlines in the Holocene, together with the recent seismicity, indicates that the deformation in the chain is still active. In the north-western portion of the chain, the seismic activity is spread along 200-300 km trending NW-SE along the seismogenic lineaments that can generate Mw 5- 6 earthquakes, exceptionally Mw 6-8 (Hatzfeld et al., 2010; Paul et al., 2010; Rajabi et al., 2011).

The Loumar slope deformation has been affecting the northeastern flank of the Gavar anticline, which represents a folded 12-14 km-thick sedimentary cover deposited on the NE continental border of the Arabian plate from Cambrian to Pliocene (McQuarrie, 2004) developed in the Zagros Simply Folded domain,. Its maximum width in the Pusht-e Kuh arc (Lorestan Arc) is 230 km and it includes about 12-14 northwest (NW) southeast (SE)-trending major whale-back anticlines (Casciello et al., 2009; Verges et al., 2011; Verges et al., 2019). The belt of anticlines is bordered south-westward, along the frontal region, by a major geoflexure, the Mountain Front Fault (MFF), whose irregular geometry defines the salient of Push-e Kuh Arc (Lorestan Arc) and the re-entrants, to NW and SE, of the Kirkuk and Dezful embayments, respectively (McQuarrie, 2004). The Mountain Front Flexure bounding the Pusht-e Kuh arc is limited by an EW-trending fault segment along the Balarud fault, a frontal segment along the Anaran anticline, and a NS-trending segment along the Khanaqin fault. The High Zagros Fault (HZF) limited north-eastward the Zagros Simply Folded belt (e.g., Verges et al., 2019). In such a geological context, the development and the evolution of fluvial network are strongly linked to tectonic folding, since the growth, lateral propagation, and linkage of individual fold segments interacts with fluvial incision and denudational processes generating high-relief hillslopes and narrow river valleys (Delchiaro et al., 2019, 2020a, 2020b). The rejuvenation of the drainage system, marked by the passage of erosional waves and by knickpoints migrating upstream, predispose the hillslopes to approach the threshold angle for landslide occurrence and the MRC deformations to initiate, eventually evolving in massive rock slope failures (Delchiaro et al., 2019).

3 Stratigraphy of the study area

The total thickness of the sedimentary succession in the Gavar anticline (Lorestan Arc) is 12-14 km and it is composed of both the passive margin sequence, lasting from the Upper Paleozoic to the Late Cretaceous, as well as of the foreland sequence, developed from Late Cretaceous to the present (Casciello et al., 2009; James & Wynd, 1965; Llewellyn, 1974; Verges et al., 2011; Verges et al., 2019). In this regard, we referred for the geological mapping (Figure 2) to the most detailed stratigraphic column proposed by Alavi (2004) and James and Wynd (1965) and to the detailed mapping conducted by the National Iranian Oil Company (Llewellyn, 1974). The 3-4 km thick Mesozoic succession testifies that the region was dominated by large carbonate platforms with associated shallow basins filled with marls, shales, and marly limestones interbedded with episodic plugs of evaporites, typical of a passive margin. It includes the carbonates of the Bangestan Group, one of the largest reservoirs for hydrocarbons in Iran, as well as the Gurpi Formation (Upper Cretaceous, thickness about 400 m) consisting of marly limestone, marl and hemipelagic shales of deep marine facies associated to the progressive migration toward the south of the pro-foreland areas, which are in unconformity with the Bangestan Group (Verges et al., 2011). Whereupon, two clastic wedges, separated by the Early-Middle Miocene carbonate of Asmari Formation, developed (Casciello et al., 2009; Verges et al.,

2011; Verges et al., 2019): the proto-Zagros foreland sequence (Paleocene-Early Eocene) and the Mesopotamian foreland succession (Miocene-Early Pleistocene).

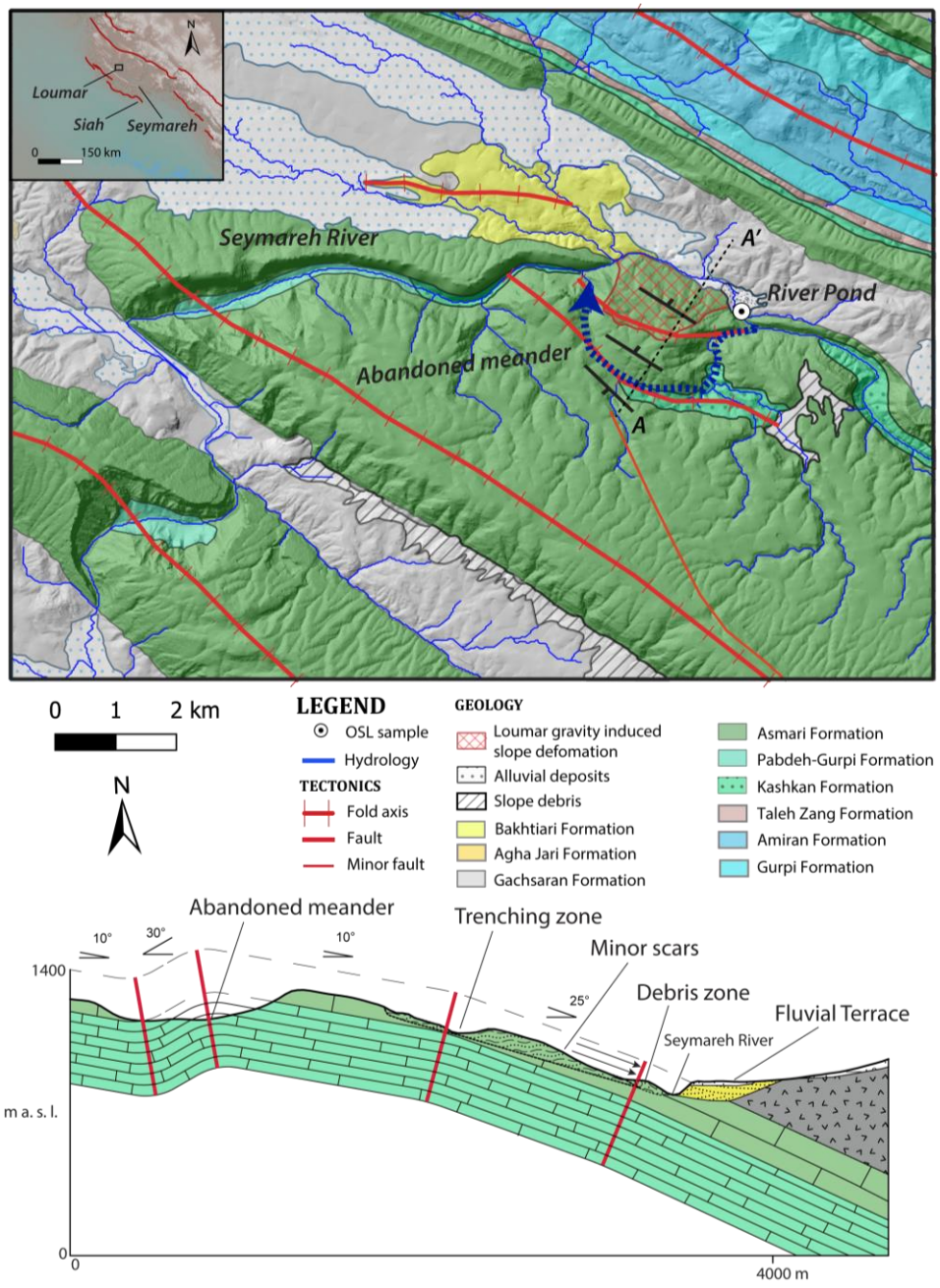

Figure 2. Geological map and cross-section of the Loumar gravity-induced slope deformation evolved in a rockslide.

The proto-Zagros foreland sequence consists of a clastic wedge filled up by a mixed carbonatic-siliciclastic sequence formed by Amiran, Taleh Zang, and Kashkan formations (Casciello et al. 2009). The Amiran Formation is formed by marly shales, sandstones, and cherty conglomerates, displaying an overall shallowing upward trend (thickness variable from 1100 m to 150 m), the Taleh Zang Formation is composed of carbonate-clastic deposits and reef

limestones (thickness variable from 350 m to 40 m) and the Kashkan Formation characterized by a continental succession formed by reddish cherty conglomerates, sandstones and mudstone (thickness variable from 400 m to 150 m). At the top of the clastic wedge, the succession is completed by the Early-Middle Miocene carbonate of Asmari Formation (thickness 200-250 m). It consists of alternating fossiliferous, massive, thinly stratified gray-brown limestone, microcrystalline limestone, dolomitic limestone, and marly limestone (Casciello et al., 2009; James & Wynd, 1965; Llewellyn, 1974; Verges et al., 2011; Verges et al., 2019). The Mesopotamian foreland succession oeverlaps the Asmari Formation . Referring to the Changuleh syncline studied by Homke et al. (2004), the foreland stratigraphy includes the following: (i) the Gachsaran Formation (Early Miocene–12.3 Ma, thickness approximately 400 m), composed of salt, anhydrite, marl, and gypsum; (ii) the Agha Jari Formation (12.3–3 Ma, thickness approximately 1400 m); and (iii) the Bakhtiari Formation (3 Ma–Early Pleistocene, thickness approximately 900 m). The Agha Jari Formation consists of sandstones and conglomerates, linked to the evolution from deltaic to fluvial transitional environments (Elyasi et al., 2014), and the Bakhtiari formation consists of conglomerates characterized by coarse and mud-supported grains, sandstones, shales and silts and marks the onset of a syn-orogenic fluvial environment (Shafiei & Dusseault, 2008).

In the Gavar anticline, the proto-Zagros foreland sequence is involved in the folding and the Asmari Formation creates a carapace covering its top, while in the synclinal valleys between the Gavar fold and the adjacent folds, the Mesopotamian foreland succession crops out extensively. Regarding the timing of the deformation, Homke et al., 2004 provide the dates of 8.1 and 7.2 Ma for the onset of the deformation in the front of the Push-e Kuh Arc (related to the base of the growth strata observed in the NE flank of the Changuleh syncline) that lasted until 2.5 Ma, around the Pliocene–Pleistocene boundary, while Verges et al. (2019) locate the onset 11.8 Ma referring to the Afrineh syncline in the inner part of the Lorestan region.

4 Geomorphological setting

Several landscape evolution models have been proposed so far to explain the drainage history of the Zagros in response to the tectonic deformation of the area. The milestone works by Oberlander (1965, 1968, 1985) explained the role of rock erodibility of the outcropping formations in the drainage evolution of the Zagros Mountains. Tucker and Slingerland (1996) computed a numerical landscape evolution model, calibrated on the Kabir-kuh fold, to understand how the growth and propagation of the folds, the different lithologies, and the drainage network could influence the sediment flux from a tectonically active belt towards the foreland basin. More recently, Ramsey et al. (2008) focused on the drainage network modifications testifying the lateral growth of the thrust-fold structures. Only a few recent studies (Delchiaro et al., 2019, 2020b) investigated the relationship among time-dependent rock mass deformations, landscape evolution rates, and tectonics as predisposing factors for massive rock slope failures. Delchiaro et al. (2019) provided insights into the causes and effects of the largest landslide and related damming that occurred on the emerged Earth surface, the giant Seymareh rock avalanche (debris-covered area of about 220 km^2), while Delchiaro et al. (2020b) presented the role of the present-day geomorphic processes in the Siah-kuh DSGSD (debris-covered area of about 8 km^2). In both cases, similar structural and geomorphic predisposing factors have been identified for such a kind of gravitational instabilities: 1) the stratigraphic setting, especially the different rheological behavior of the Asmari and the Pabdeh-Gurpi formations that induces differential strain rates within the slope and justifies the strain evolution toward paroxysmal

failure according to a MRC process; 2) the structural setting, moderately dipping downslope (15°-20°) reduced lateral confining effect due to continental and epi-continental deposits also reducing the vertical thickness of the carbonate Asmari Formation caprock; 3) the relief conditions, in terms of relief energy; 4) the rock mass kinematic release, necessary for the initiation of the MRC process. The estimated starting time for MRC varies from 10^1 ka (for the Siah-kuh case) to 10^2 ka (for the Seymareh landslide).

In this context, the gravitational deformation of Loumar slope represents a further and not yet investigated case history to better understand the role of tectonics and landscape evolution in predisposing the development of the MRC process. The gravity-induced slope deformation covers an area of about 3 km^2 and is located along the NE flank of the Gavar fold. The evolution of the gravity driven instability could be closely connected to the vertical and lateral growth of the anticline and to the evolution of the Seymareh River drainage system. In particular, the erosional rejuvenation of the drainage network due to the fold growth allowed the kinematic release of the Asmari caprock, both at the top and toe of the slope, likely causing the initiation of the deformational process.

5 Methods

The Gavar fold area was firstly investigated through the analysis and interpretation of remote sensing data, such as Google Earth satellite optical images (2018 Landsat Imagery) and vector topographic maps (National Cartographic Center of Iran, topographic map of Kuhdasht, scale: 1 : 25 000), which led to the first detection of possible geomorphic markers along the fold and the surrounding areas. Vector topographic data also allowed the computation of a 10 m digital elevation model (DEM) for terrain analyses and led to the projection of the possible geomorphic markers along the river longitudinal profile (Burbank & Anderson, 2012; Wilson & Gallant, 2000). The DEM was obtained by the ArcGIS 10® software package, starting from vector topographic data (contour lines, hydrography, and point elevation) and using the ANUDEM interpolation algorithm (Hutchinson et al., 2011, and references therein). The drainage network was extracted and analysed using TopoToolbox (Schwanghart & Scherler, 2014) and the Topographic Analysis Kit (TAK) by Forte and Whipple (2019), both sets of Matlab functions for topographic analysis. We performed the inverse modeling of the longitudinal profiles of the drainage network using a Matlab code gently provided by Sean Gallen. The SARscape software tool was used to apply satellite SAR Interferometry. Finally, a geological and geomorphological field survey was carried out with the aim of mapping the most significant active and relict landforms for the Quaternary evolution of the Seymareh River valley and of sampling the corresponding deposits for dating with the OSL method (optically stimulated luminescence; Murray & Olley, 2002; Wintle & Murray, 2006; and references therein).

More in detail, to accomplish the purpose of inferring the Quaternary tectonic and landscape evolution of the Gavar fold as well as the chronology of the events that led to the gravitational deformation assessing the related present-day residual activity and risk, it was necessary to:

1) perform a basin-scale geomorphometric analysis of the Seymareh River basin and the Gavar anticline;

2) apply the inverse modeling to the drainage network calibrating the parameters at the fold-scale with a sensitivity analysis;

3) reconstruct the main morpho-evolutionary stages of the river valley, which have been constrained by the OSL dating of a river deposit caused by the Loumar landslide and by the plano-altimetric distribution of other geomorphic markers;

4) quantify the ground displacement rate through space-borne SAR Interferometry to assess the residual activity related to the Loumar landslide.

5.1 Remote and field surveying

A remote survey was carried out to map the gravity-induced landforms, based on the Google Earth satellite images (2018 Landsat Imagery); a field cross-check was also performed. Specifically, during the geological and geomorphological field survey, the mapping of the most significant active and relict landforms for the Quaternary evolution of the Seymareh River valley, as well as the sampling of the river pond deposit to be dated with the OSL method (Optically Stimulated Luminescence; Murray & Olley, 2002; Wintle & Murray, 2006; and references therein), were carried out. OSL sampling is a very delicate and quite complex technique. In fact, it is absolutely necessary to prevent the sample from being exposed to light because the luminescence signal could be reduced or even reset. In choosing the most suitable site to sample, of course, levels were identified with original sedimentary structures, avoiding bioturbations and post-depositional alterations. Once the site for sampling was identified, it was important to carefully clean off the slope and prepare, according to the consistency or cementation of the material, the equipment necessary for taking the sample, without it being exposed to light. Furthermore, to minimize the effects of cosmic radiation and to thereby avoid the risk of rejuvenated ages, the samples were taken at least one meter below the topographic surface (or below eventual erosional surfaces identified within the deposits). The soil, mainly characterized by fine-grained loose sediments (size <2 mm) was sampled by a hammer to insert a metal tube horizontally into a vertical face, which must be isolated from light and humidity immediately after collection. To maximize the uniformity of the natural radioactivity of the burial period, the tube was inserted into zones of homogeneous sediment at least 30 cm wide and thick. From the same level where it was sampled, an additional 500–800 g of sediment was extracted to evaluate natural radioactivity (if the annual dose rate measurement is not performed in situ), for the mineralogical and granulometric analysis, as well as to determine the moisture content. The OSL dating was performed by the LABER OSL Laboratory, in Waterville, Ohio, USA. Quartz was extracted for the equivalent dose (De) measurements. In the OSL laboratory, the sample was treated first with 10 % HCl and 30 % H2O2 to remove organic materials and carbonates, respectively. After grain-size separation, the fraction of 90–125 μm size was relatively abundant, so this fraction was chosen for De determination. The grains were treated with HF acid (40 %) for approximately 40 min to remove the alpha-dosed surface, followed by 10 % HCl acid to remove fluoride precipitates. Luminescence measurements were performed using an automated Risø TL/OSL-20 reader. Stimulation was carried out by a blue LED (λ=470±20 nm) stimulation source for 40 s at 130 °C. Irradiation was carried out using a 90Sr/90Y beta source built into the reader. The OSL signal was detected by a 9235QA photomultiplier tube through a U-340 filter with a 7.5 mm thickness. For De determination, the single-aliquot regenerative-dose (SAR) protocol (Murray & Olley, 2002; Wintle & Murray, 2006) was adopted. The preheating temperature was chosen to be 260 °C for 10 s and then cut heat was 220 °C for 10 s. The final De is the average of the De of all aliquots, and the final De error is the standard error of the De distribution. For each sample, at least 12 aliquots were measured for De determination. The De was measured using SAR on quartz, and the aliquots

that passed criteria checks were used for final De calculation. Recycling ratios were between 0.90–1.1, and recuperation was relatively small. The cosmic ray dose rate was estimated for each sample as a function of depth, altitude, and geomagnetic latitude. The concentration of U, Th, and K was measured by neutral activation analysis (NAA). The elemental concentrations were then converted into the annual dose rate, considering the water content (lab measured) effect. The final OSL age is then De/Dose rate.

5.2 Geomorphometric analysis

The drainage network was extracted and analysed using TopoToolbox (Schwanghart & Scherler, 2014) and the Topographic Analysis Kit (TAK) by Forte and Whipple (2019). The flow accumulation threshold was set according to that proposed for the fluvial domain (10^{-1} km^2) by Montgomery and Foufoula-Georgiu (1993) in order to conduct analyses uniformly for the whole Seymareh River basin. The geomorphometric analysis was focused on the Seymareh River basin, closed at the confluence with the Karkheh River. The drainage area of the basin is 41,244.8 km^2. Then, the main catchment was subdivided using the trunk option of the SubDivideBigBasins function of TAK, which uses the tributary junctions with the trunk stream within the main basin as pour points for sub-basins. Accordingly, 2319 sub-basins were obtained and for each of them the hypsometric curve and integral were derived in order to distinguish relatively "young" or weakly eroded regions (with convex curves with HI values close to 1) and relatively "old" or highly eroded regions (with concave curves and HI values close to 0), as well as other topographic metrics based on the stream power law and following derivations (k_s, k_{sn}, χ; Howard & Kerby, 1983; Perron & Royden, 2013; Whipple & Tucker, 1999). Moreover, the *mnoptim* function of TopoToolbox was used to obtain the best mn-ratio for the stream power law. Such a function uses Bayesian Optimization with cross-validation to find a suitable mn-ratio. Bayesian Optimization finds a minimum of a scalar-valued function in a bounded domain. Specifically, the mnoptim uses χ (Chi) analysis (Perron and Royden, 2013) to linearize long-river profiles. If there are several river catchments (or drainage network trees), the function will pick a random subset of these trees to fit a mn-ratio and then tests it with another set of drainage basins. This allows to assess how well a mn-ratio derived in one catchment can actually be applied to another catchment. In this regard, we chose to refer the value to the whole drainage basin deriving a mn-ratio that applies best to all sub-basins.

5.3 Linear Stream Power Law (SPL) for fluvial inverse modelling

In detachment-limited conditions, typical of tectonically active regions, the evolution of the river profile is described by the stream power law (SPL) as the change in elevation z of a channel point x through time t (Howard & Kerby, 1983), which relates to the competition between erosion (E) and uplift (U):

$$\frac{dz(x,t)}{dt} = U(x,t) - E\,(x,t) \tag{1}$$

where fluvial erosion E is computed as:

$$E\,(x,t) = K\,A\,(x)^{\,m}\left(\frac{dz\,(x,t)}{dx}\right)^{n} \tag{2}$$

The powers *m* and *n* are positive constants controlling the erosion mechanism. Specifically, *m* depends on the climatic conditions and hydraulic properties of the discharge, and *n* is a function of other erosional thresholds (Di Biase & Whipple, 2011; Whipple & Tucker, 1999). The erodibility, *K*, accounts for the lithology, the climatic conditions, and the channel geometry. In the general case, *K* can vary in space and time, but in the treatment presented here, it is taken as a constant. A power-law relationship between the local channel slope (*S*) and the upstream drainage area (*A*) reveals the steady-state river profile:

$$S\,(x,t) = \left(\frac{E(x,t)}{K}\right)^{\frac{1}{n}} A(x)^{-\frac{m}{n}} = k_s\,A(x)^{-\theta} \tag{3}$$

where $k_s = (E\,(t, x) / K)^{1/n}$ is known as the steepness index and *mn* ratio or θ is defined as concavity index. According to the steady-state conditions, the surface elevation, the erosion rate, and the relative uplift rate do not vary over time, $U(x)= E(x)$, $n=1$ and the steepness index takes the form (Kirby & Whipple, 2012):

$$k_s = \frac{E\,(x,t)}{K} = \frac{U(x,t)}{K} \tag{4}$$

If *U* and *K* are space-invariant, we can perform the integration of $(U/K)^{1/n}$ from a base level x_b to an arbitrary upstream point *x* of the channel to predict the elevation of a river profile (Perron & Royden, 2013):

$$z(x) = z(x_b) + \left(\frac{U}{K{A_0}^m}\right)^{\frac{1}{n}} \chi \tag{5}$$

where A_0 is an arbitrary scaling area and χ is an integration of river horizontal coordinates defined by the equation:

$$\chi = \int_{xb}^{x} \left(\frac{A_0}{A(x')}\right)^{\frac{m}{n}} dx' \tag{6}$$

The erosional wave celerity, $C(x) = K\,A(x)^m\,S(x)^{n-1}$, controls the speed at which perturbations travel along the channel (Whipple and Tucker, 1999). The response time, $\tau(x)$, for perturbations to propagate from the river outlet, at $x = 0$, to a point *x* along the channel is expressed as (Whipple & Tucker, 1999):

$$\tau(x) = \int_0^x \frac{dx'}{C\,(x')} = \int_0^x \frac{dx'}{K\,A\,(x')^m\,S\,(x')^{\,n-1}} = \frac{\chi\,(x)}{K\,{A_0}^m} \tag{7}$$

where x' is an integer variable. The response time, $\tau(x)$, increases constantly with *x*, from the base level to the high channel reaches. τ-plot is the starting point for the linear inverse scheme to study the rock-uplift/base-level fall history recorded in the fluvial topography (Di Biase &

Whipple, 2011; Whipple and Tucker, 1999). Anyway, the mathematical expression of the current river elevation can be reported as (Goren et al., 2014):

$$z(x) = \int_{-\chi\,(x)}^{0} U^*\,(t^*)dt^* \tag{8}$$

where

$$t^* = K\,{A_0}^m t\;U^* = \frac{U}{K\,{A_0}^m} \tag{9}$$

The parameters t^* and χ are in units of length, and U^* is a dimensionless rate of rock uplift. Along the channel profile on the χ-z plot, the slope of different channel segments represents the corresponding channel steepness (k_s). The time scale to invert river longitudinal profiles is decided by the recession rates of the knickpoints within the drainage basin. The less the erosional coefficient (K) is, the longer history we can finally decode. Meanwhile, it takes more time for knickpoints to migrate along longer river channels, but as those channels are mostly of bigger contributing area and associated discharges, thus, knickpoints retreat faster. Therefore, a balance between higher recession rate of the knickpoints and higher discharge in setting the time scale of inversion can be expected. Rates of tectonic uplift and incision into bedrock are irrespective to the time scale of inversion, which is decided by the horizontal, not vertical recession rate of the knickpoints (Wobus et al., 2006).
Finally, it was assumed a spatially constant K and U as in a block uplift scenario employing the inverse approach stream power model solution proposed by Goren et al. (2014) and Gallen (2018).

5.4 Advanced SAR Interferometry

Satellite SAR Interferometry analysis was performed to detect any active, gravity-induced deformation of the slope already affected by the gravity-induced slope deformation. A multi-image interferometric approach was chosen, which uses many images (STACK) characterized by the same acquisition geometry to create interferograms related to a given area (Berardino et al., 2002; Bert, 2006; Ferretti et al., 2000, 2001; Hanssen, 2005). Among the various techniques, the Persistent Scatterer Interferometry (PSI) (Ferretti et al., 2000, 2001) analysis was used, based on the observation of time and space-coherent pixel, the so-called persistent scatters, represented by anthropogenic and natural structures like buildings, antennas, exposed rocks, etc. The SARscape software tool was used to process 86 Sentinel-1 SAR (Synthetic Aperture Radar) images for the ascending orbit in the time frame between 08 June 2016 and 08 November 2019, as well as 95 Sentinel-1 SAR images for the descending orbit in the time frame between 16 May 2016 and 21 November 2019. A coherence threshold of 0.7 has been used to obtain an improvement in the signal-noise ratio but guaranteeing at the same time a good PS (Persistent Scatter) density. Then, the decomposition of vertical and horizontal displacements was performed by combining PS InSAR ascending and descending data by using a proprietary software kindly provided by NHAZCA S.r.l.

6 Results

6.1 Remote and field surveying

A remote survey of the gravity-induced landforms was carried out in the Loumar area, based on the Google Earth satellite images (2018 Landsat Imagery) and followed by a field survey, during which it was possible to sample a river pond deposit identified upstream of the gravity-induced deformed slope, for OSL dating.

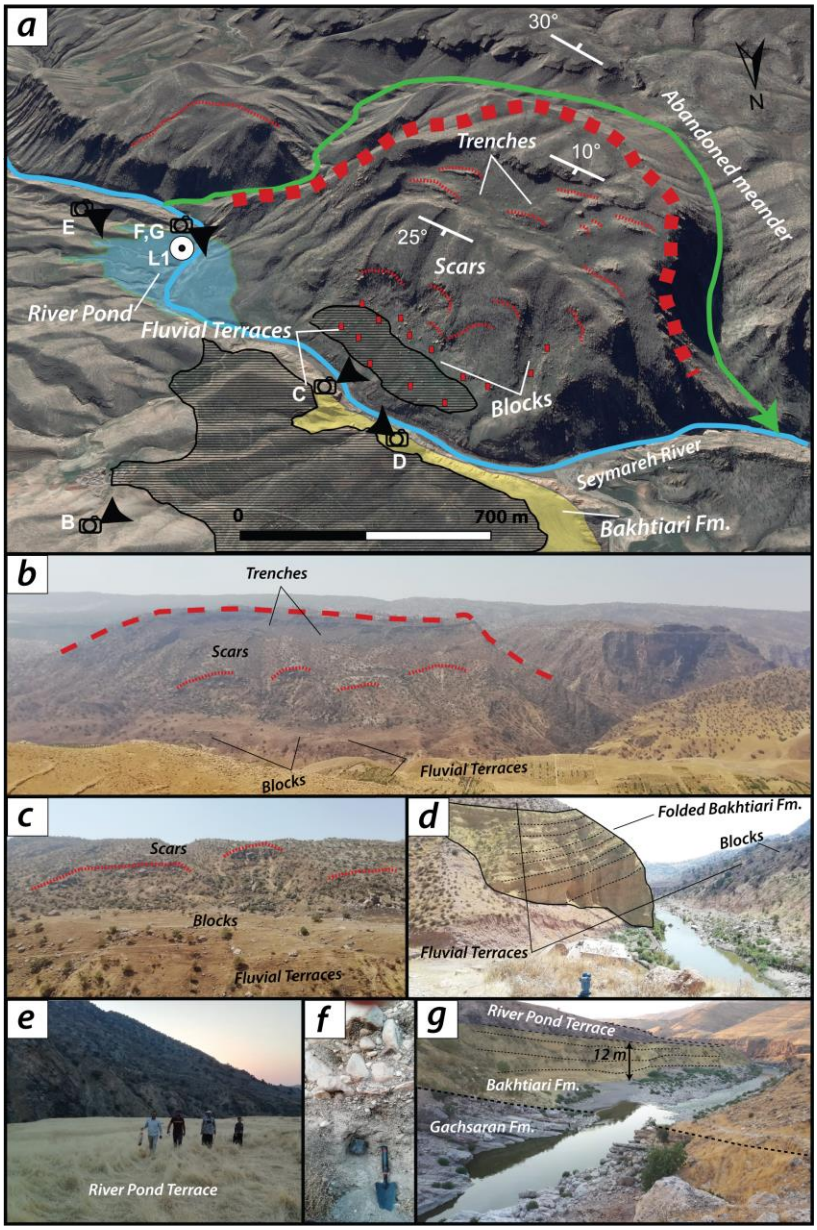

Figure 3. Google Earth satellite general perspective of area (**a**) and pictures were taken during the field survey performed in August 2019 (**b-f**) which represent different typologies of gravity-induced landforms and stratigraphic relationships.

The results of the analyses allowed to recognize and distinguish areas of the deformed slope characterized by different gravity-induced landforms as well as to define the stratigraphic relationships between the Quaternary deposits and the outcropping formations in the neighbouring areas. In Figure 3a, the general perspective of the Loumar gravity-induced slope deformation is reported, along with the evidence of its evolution into a viscous rockslide. It is possible to identify: 1) a trenching zone; 2) minor scars along the 25° dipping slope; 3) a debris zone where blocks detached from the slope accumulated. The first zone involves the Asmari Formation just below the upper limit of the deformed area and the trenching was likely favoured by the tensional release due to the change of dip-slope strata angle from 10° to 25°. The width of this zone, as well as the north-eastward deflection of the Seymareh River, suggest that the gravity-induced slope deformation likely reached the tertiary phase of MRC evolving to a viscous rockslide. In the second zone, blocks of Asmari Formation detached from minor scars and accumulated in the third area. As confirmed by the field survey (Figures 3b and 3c), the blocks accumulated above a strath terrace surface recognizable on both sides of the river at around 850 m a.s.l. The latter is sculpted on the folded strata of the Bakhtiari Formation (Figure 3d), whose thickness is decreasing from SE to NW. Upstream of the Loumar landslide, a river pond deposit at 810 m a.s.l. was detected by remote and confirmed by the field survey to lie upon the Bakhtiari Formation (Figures 3e-g). It consists of a coarsening upward deposit with a variable thickness (up to 2 m) along the present river gorge. The deposit is composed mainly by sand and silt with increasing gravel towards the top (Figures 3f and 3g). It can be related to a narrowing of the valley floor of the river due to the displacement associated to the viscous rockslide, which has led to a local loss of river erosive power. We sampled the basal, finer deposit and the obtained OSL age is 5.52±0.36 ka. This age constrains the evolution of the MRC driven gravity-induced slope deformation to a rockslide. This age can be reasonably used to calculate the minimum river erosion rate affecting the bedrock (Bakhtiari Fm.) after the landslide emplacement, which corresponds to the uplift rate over the last ~5.52 kyr. The ratio between the thickness of the eroded bedrock below the terrace surface (~12 m) and the time elapsed since the initiation of the erosional phase (~5.52 kyr, which is overestimated) allowed us to obtain a minimum uplift rate for the last 5 ka of 2.18 ± 0.14 mm yr^{-1}. The remote analysis allowed also to identify an abandoned meander of the Seymareh River (Figure 3) which flowed upstream of the deformed area where the Asmari Formation strata attitude changes from 30° SW to 10° NE, to form a parasitic anticline along the NE flank of the Gavar fold. The growth of the parasitic fold was likely linked to the lateral propagation of the entire structure, which helped the meander abandonment. This change in the river course allowed the kinematic release of the NE flank of the Gavar fold, likely giving the start to the MRC deformation process. Further evidence of such stream piracy is a knickpoint cluster related to the NE Loumar drainage network at 1050 m a.s.l., which is described in the following section.

6.2 River basin metrics

The whole Seymareh river basin was firstly analysed and then the local drainage associated with the Gavar fold was focused on, in order to evaluate some geomorphometric parameters on which the fluvial inverse modelling was then built. Specifically, the hypsographic curve and the hypsometric integral (HI) were computed for each sub-basin of the whole Seymareh river basin. Then the best mn-ratio was obtained by applying Bayesian Optimization. At the fold scale, the computation of the k_{sn} index, as well as the analysis of the longitudinal profiles and their knickpoints was performed. In Figure 4, the HI values for each of the 2319

sub-basins of the Seymareh river basin are reported (the normalized area-height curves are collected in the supplementary material). The normalization of the curves and the HI values allow to compare drainage basins with different size, since area and elevation are plotted as functions of total area and total elevation.

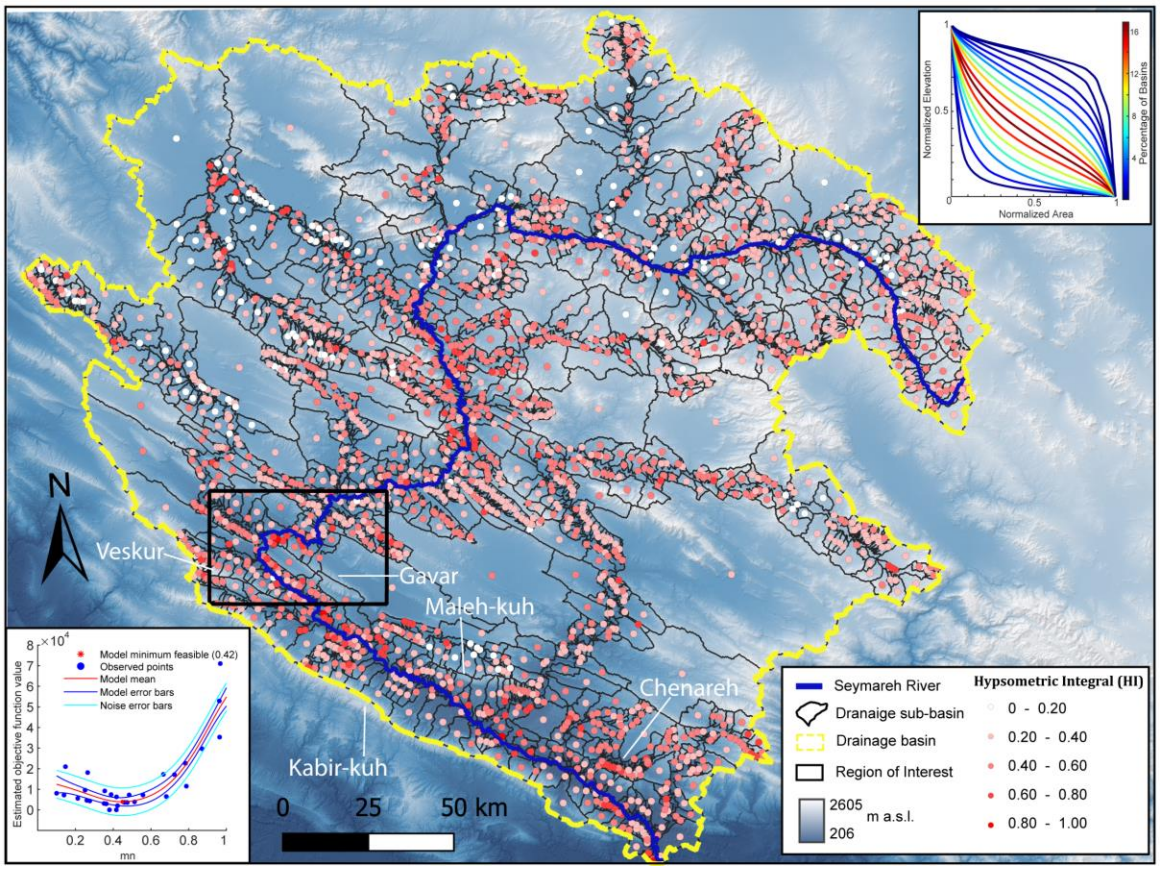

Figure 4. Seymareh River basin and sub-basins with the calculated values of Hypsometric Integral (HI). The results of the Bayesian Optimization performed for finding a suitable mn-ratio are also reported.

The shape of the hypsometric curve as well as the area below the hypsometric curve known as the hypsometric integral (HI), that varies from 0 to 1, provide information about the erosional stage of the drainage basins. They also provide valuable information about the tectonic, climatic, and lithological factors controlling the catchment landscape. Anyway, convex hypsometric curves and HI values close to 1 characterize relatively “young” or weakly eroded regions, S-shaped curves and HI values close to 0.5 moderately eroded regions, while concave curves and HI values close to 0 relatively “old” or highly eroded regions. Most of the curves (81.1%) have an S-shape morphology with HI values ranging from 0.3 to 0.7; concave shape morphologies with HI values ranging from 0 to 0.3 are 17.1 %, convex shape ones with HI values ranging from 0.7 to 1 are only 1.2%. Figure 4 shows that the highest HI values are located along the main fold structures (Kabir-kuh, Chenareh, Maleh-kuh, Veskur, Gavar) where the tectonic uplift is likely still acting (Casciello et al., 2009; Verges et al., 2011) while the lowest are distributed especially along the main alluvial valley where the landscape has experienced erosion since a long time. In Figure 4 the results of the Bayesian Optimization with cross-

validation to find a suitable mn-ratio are also reported. The function picked 34 random drainage network trees to fit a mn-ratio, by testing them with another set of drainage basins. The minimum of the estimated objective function value is 0.42. The high density of observed points around this value indicated the good reliability of the result.

Longitudinal river profiles and knickpoint analysis can be interpreted as resulting from the balance between rates of erosion and uplift. Concave-up profiles represent long-term equilibrium between uplift and erosion rates. Concave-convex profiles with erosion steps in the middle reaches indicate a long-term predominance of erosional processes. Convex profiles are characteristic of areas where active tectonics (uplift) is dominant. In this regard, a plano-altimetric analysis of the major knickpoints of the Gavar fold drainage network was performed (Figure 5a). The knickpoints were classified by their elevation drop and projected along the longitudinal profiles of the streams located in different parts of the fold, respectively at NE, NW, SE, and SW (Figure 5b). The knickpoint histogram in Figure 5c shows quite well at least 3 main clusters of knickpoint by elevation: the first at about 1580 m a.s.l., the second at about 1400 m a.s.l. and the last one at about 1050 m a.s.l. Each cluster is characterized by high knickpoint drop that reaches 150-192 m. In general, all the knickpoints are associated with the presence of a large anomalous patch of low relief/slope landscape. But the low relief areas are especially visible in the SE and SW Loumar drainage networks while in the NE and NW sectors of the fold the patches are increasingly steeper towards NE. In Figure 5, the density distribution of the steepness index, k_s, is shown. It was computed on the Gavar fold drainage network using the obtained value of channel concavity (or mn-ratio) of 0.42. The mean value of ks is 53.68 with a standard error of 0.76. Moreover, we projected along the swath profile of the Gavar fold axis the knickpoints distinguished by the elevation drop and the HI value of the drainage sub-basins associated to their centroids, as geomorphic markers of the fold growth (Figure 5d). The swath profile represents the trends of maximum, minimum, and mean elevations and therefore shows all the wavelengths of topography. The gap between the maximum elevation and the minimum elevation is proportional to the erosional stage of the examined sector and the morphology of the minimum curve is an indicator of the activity of the process that generated it. In this regard, along the fold, it is possible to recognize 4 V-shaped valleys, whose flowing direction is NE-SW, orthogonal to the axis of the fold. They include the water gaps of the Seymareh River and the SE Loumar drainage network, respectively in the NW and SE zones of the tectonic structure, while the valleys in the middle portion of the profile correspond to wind gaps. Generally, the water gaps are frequent in the closing area of a growing fold with lateral tip migration and are characterized by a narrow V-shaped cross-profile, since the fluvial process is still acting, while the wind gaps are typical of the most central part of the anticlines and have an open V-shaped profile because of the inactivity of the fluvial incision. The gap between the maximum elevation and the minimum elevation is greater in the wind gaps as the erosional stage is advanced compared to the water gaps in which the erosive action is younger. When a fold starts growing laterally, the rivers erode the raised area or, otherwise, they are deflected from their course and forced to flow around the fold periclinal closure. If the erosion rate of the river is higher than the uplifting rate, a water gap is set up, otherwise its course is deflected generating a wind gap. Even the elevation of the valley floors along the swath profile testifies to a greater and older uplift of the central part of the fold and a subsequent lateral growth towards NW and SE, respectively. The average elevation of the water gaps stands at 800 and 1400 m a.s.l. respectively for the Seymareh River and the SE Loumar drainage network while that of the wind gaps is around 1620

m a.s.l. The projections along the swath profile of the Gavar fold axis in Figure 5d confirms the hypothesized propagation of the fold in the NW direction.

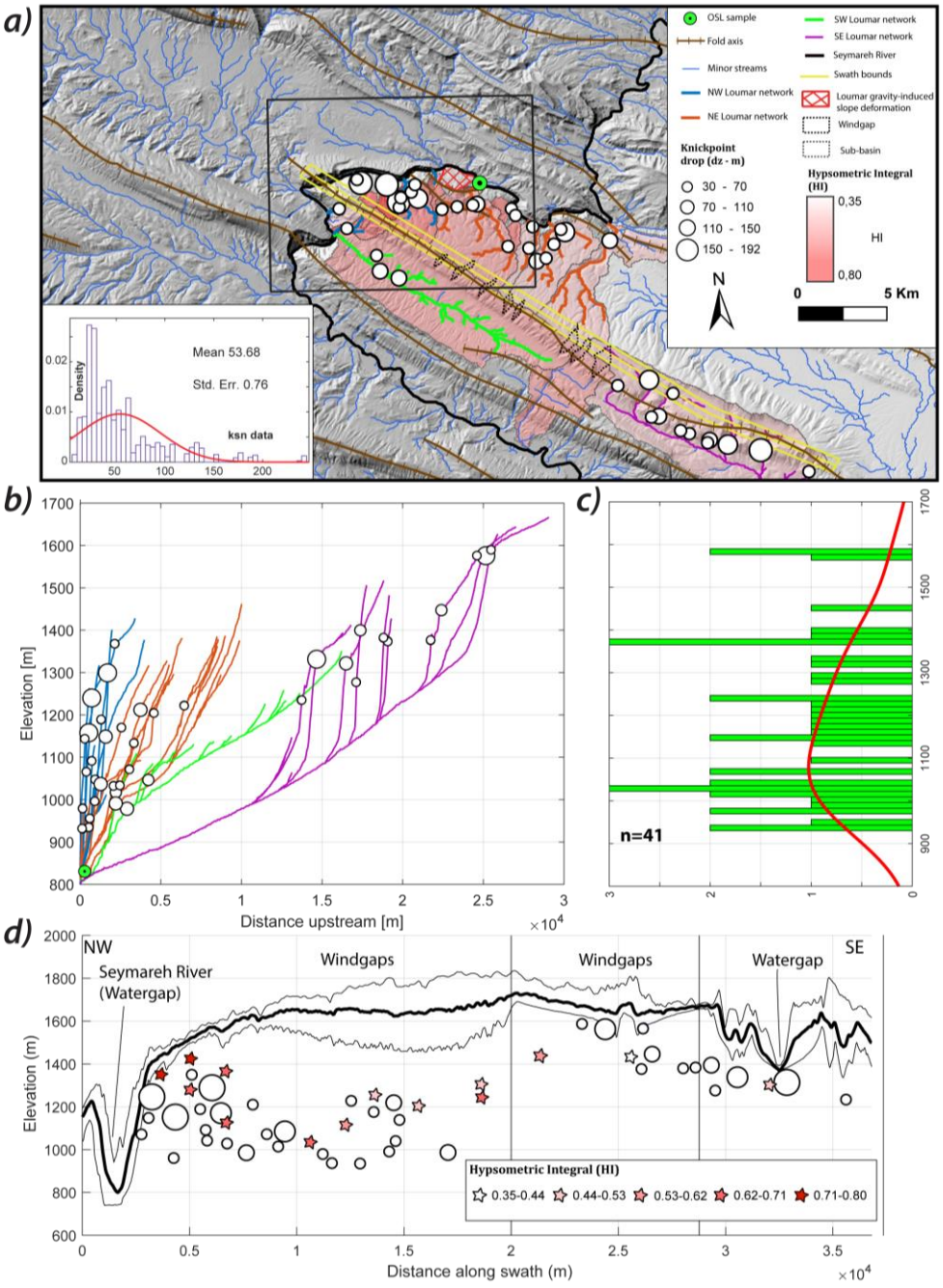

Figure 5. Hillshade showing the Seymareh River valley and drainage network associated with the Gavar anticline (**a**). Longitudinal profiles (**b**) and histograms of the distribution of knickpoints elevation (**c**) and the swath profile along which geomorphic markers are projected (**d**) are reported.

As it regards the plano-altimetric distribution of knickpoints, two elevation clusters can be distinguished. Specifically, the first characterizes the NW termination of the fold at elevations

between 1400 and 900 m a.s.l. with the highest elevation drops around 1200 m a.s.l. On the other hand, the second cluster is defined in the SE part of the fold, reaching higher altitudes between 1600 and 1300 m a.s.l. In the latter, the higher elevation drops are associated with the SE-ward wind gap and the SE Loumar drainage network, respectively at an altitude of around 1600 m and 1350 m a.s.l.Finally, the HI value distribution of the drainage sub-basins associated to their centroids corroborates the hypothesized fold growth and propagation of the tips. In fact, a trend of HI values along the fold axis is evident. Specifically, the sub-basins are characterized by high values (0.80) in the NW part and by low values in the SE part (0.47) with a minimum peak associated with the wind gap located to SE (0.36). This distribution of values demonstrates the river rejuvenation within the sub-basins developed close to its tips, especially in its NW part.

6.3 Inverse modelling

In this analysis a linear dependency between the local slope, *S*, and the erosion rate, *E*, in the stream power erosion model was assumed according to equation 3, i.e., the slope exponent, $n = 1$. When $n \neq 1$, river reaches are consumed or generated along slope breaks (Royden and Perron, 2013), a situation that is interpreted as shock behavior (Pritchard et al., 2009). In agreemen with Pritchard et al. (2009), shocks occur when a steeper reach of the river, which is propagating rapidly upstream, overtakes a less steep reach, which is propagating more slowly upstream.

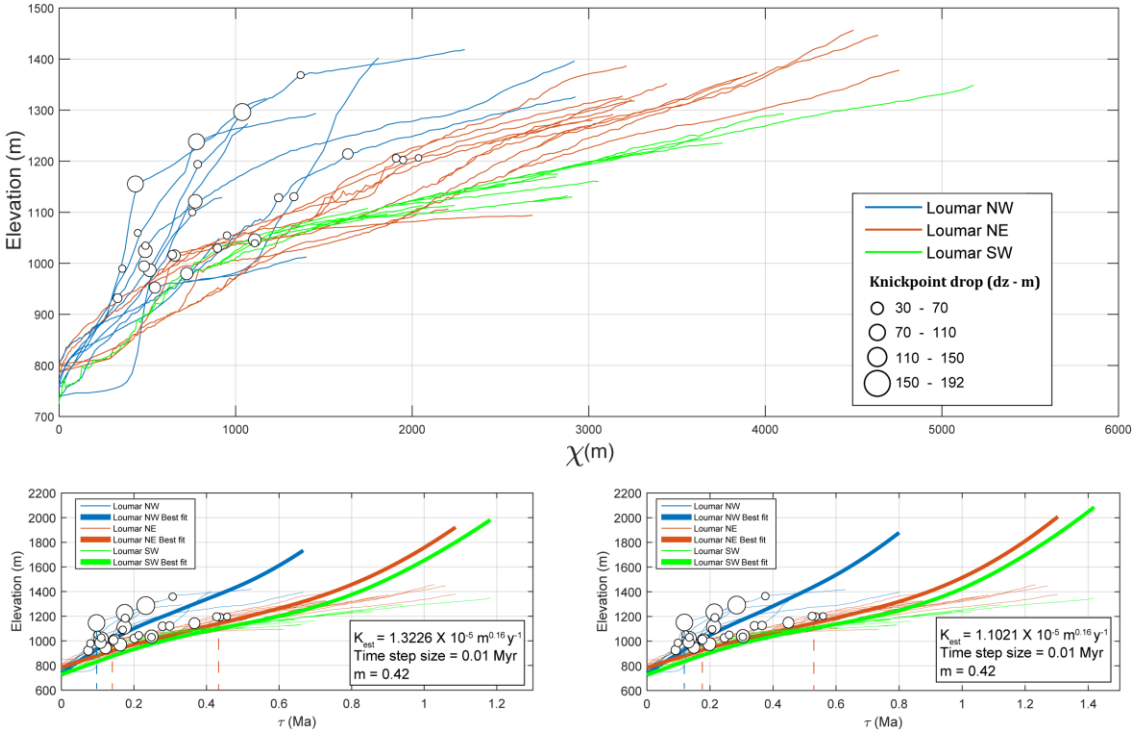

Figure 6. χ-plot of the drainage networks of the Gavar fold with the relative empirical and best fit τ-plots computed for K_{max} and K_{min}.

However, in our case the tectonic perturbation is not expected to be shocking and impulsive as in a fault case since we are dealing with a folding style. An additional key assumption that we adopt in the current analysis is that the drainage area of the fluvial channels is fixed during the history that is represented by the long profiles of the rivers. Area change can

take the form of stream piracy, migration of the main water divide, or migration of the lateral divides between the analyzed basins.

In this regard, the evidence of river piracy can be traced back to a period prior to the one studied as they are located along the heads of the network considered in the analyzes. Such an assumption is not only important for the correct inference of the uplift rate history but also for constraining the *m* exponent correctly. For this reason, the *m* coefficient was calculated at the scale of the whole main basin and cross validated between the different sub-basins. We performed the linear inversion of all the drainage networks affecting the Gavar fold, except for the SE Loumar network because its outlet is too high.

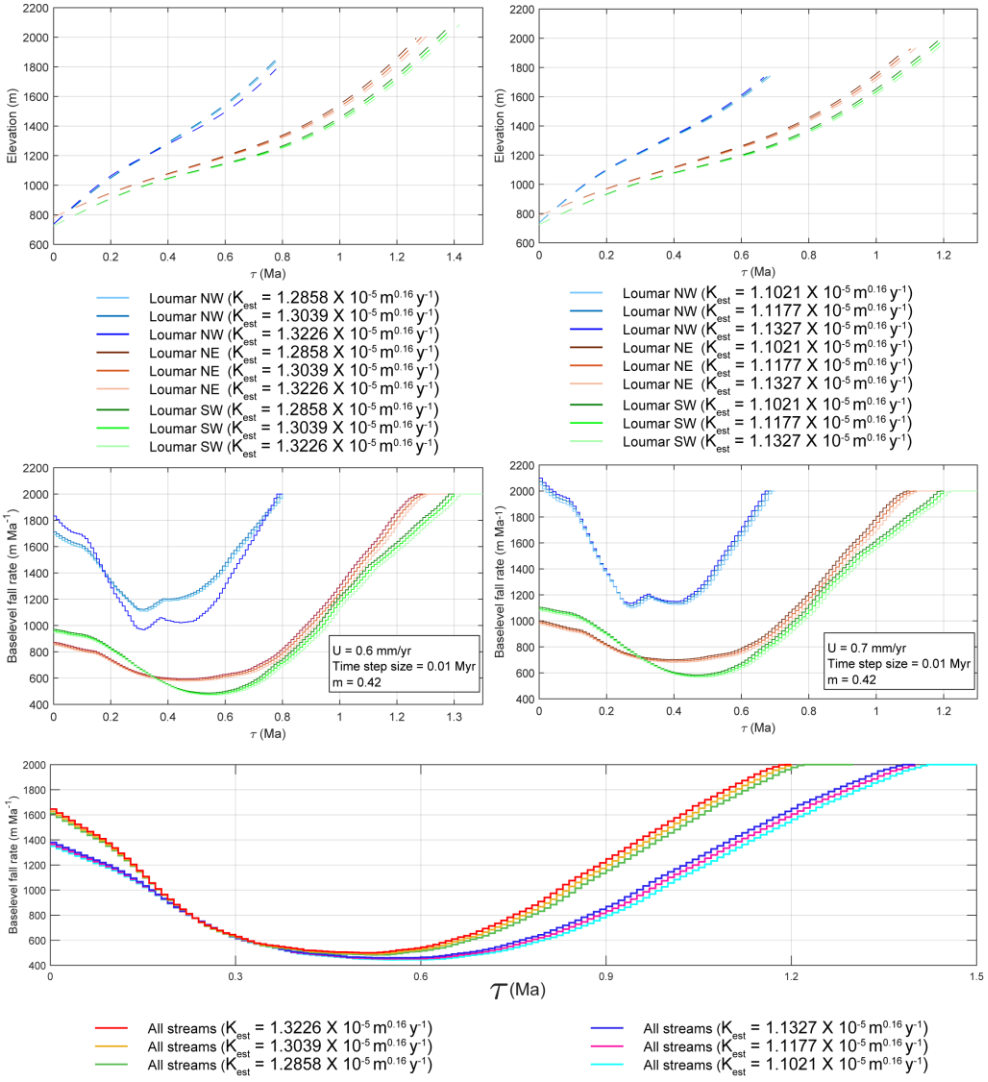

Figure 7. Best fit τ-plots and relative linear river inversion curves computed for each drainage network and all the K_{est} are reported. Linear river inversion curves of the entire draining system for all the K_{est} is also shown.

In this regard, the streams at the confluence with the Seymareh River that were not suitable for the SE Loumar system were trunked. In order to provide a sensitivity analysis and calibrate the erodibility *K*, equation 4 was applied, considering different uplift rates and a range

of k_s values. On one hand, literature data about the uplift rate affecting the Zagros Mountains were taken into account to assume an averaged regional uplift rate ranging between 0.6 and 0.7 mm y^{-1}, used respectively in the Kurdistan (Tozer et al., 2019; Zaberi et al., 2019) and Fars area (Yamato et al., 2011). On the other hand, the mean value of k_s which is 53.68 with a standard error of 0.76 was assumed. In this way, 6 different values of K_{est} were obtained: 1.2858 e^{-5} $m^{0.16}$ y^{-1}, 1.3039 e^{-5} $m^{0.16}$ y^{-1}, 1.3226 e^{-5} $m^{0.16}$ y^{-1} dividing the uplift rate 0.7 mm y^{-1} by the max, the mean and the min k_s values, respectively; 1.1021 e^{-5} $m^{0.16}$ y^{-1}, 1.1177 e^{-5} $m^{0.16}$ y^{-1}, 1.1337 e^{-5} $m^{0.16}$ y^{-1} dividing the uplift rate 0.6 mm y^{-1} by the max, the mean and the min k_s values, respectively. The inversion results were, then, calibrated using the values of K_{est} and m (being $n = 1$ for the steady-state condition then $\theta = m$) equal to 0.42 as a result of mn-ratio Bayesian Optimization with a time step size of 10 ka. In Figure 6, the stream network elevation was reported in χ space and converted in τ space for K_{max} and K_{min}, by applying equation 7. We referred to the max and min K in order to obtain the largest time windows of the main tectonic events affecting the fold. We calculated them dividing the maximum uplift rate and the min k_s by K_{max}, the minimum uplift rate, and the maximum k_s by K_{min}. In the τ curves computed singularly for each stream network, the response time, $\tau(x)$, for perturbations to propagate is plotted against the elevation. Therefore, knickpoints can be associated with perturbations that can be time constrained. It was possible to recognize: 1) a first tectonic event at 0.46 ±0.04 Ma associated to the knickpoint cluster of the NW Loumar network at around 1200 m a.s.l.; 2) a second tectonic event at 0.16 ±0.015 Ma referable to the meander abandonment by the Seymareh River associated to the development of the knickpoints cluster along the NE Loumar drainage network at 1050 m a.s.l.; 3) a third tectonic event at 0.11 ±0.01 Ma responsible of the recent lateral propagation of the fold towards NW, highlighted by the knickpoint cluster along the NW Loumar network at about 1170 m a.s.l. Regarding the linear river inversion curves under the block uplift assumption, in Figure 7 the tectonic history (that was generically interpreted as base-level fall rate increases) at the outlet point of the drainage systems at the confluence with the Seymareh River, are reported. Specifically, the best-fit τ-plots and relative linear river inversion curves was computed for all the K_{est} referring to each drainage network as well as to the entire Gavar fold draining system. Figure 7shows that the tectonic history is as much long as K_{est} is greater, ranging from 1.2 Ma with K_{max} to 1.4 Ma with K_{min}. Moreover, the base-level fall rates are greater increasing K_{est}: the difference between K_{max} and K_{min} increases from 0 at the inversion start time to at least 0.2 mm yr^{-1} at present-day. Regardless the parameters chosen for the modelling, the tectonic history relating to the NW Loumar drainage network is shorter and characterized by a more intense base-level fall rate than that of the other portions of the fold. In fact, the Loumar NW sector started to uplift ranging from 0.75 ± 0.05 Ma compared to NE and SW sectors, which were involved in folding respectively at 1.2 ± 0.05 Ma and 1.3 ± 0.1 Ma. Generally, the influence on the estimation of the parameter K by the uplift rate and that by k_s depends on the order of magnitude of the variability of the parameter in question. In fact, it must be highlighted that both time and base-level fall rate variability is determined primarily by the uplift rate value and secondly by the k_s. According to the linear inversion curves performed for the entire Gavar fold drainage network (Figure 7), the fold experienced on average about 1.3 ± 0.1 Myr of tectonic history. From 1.3 ± 0.1 to 0.54 ± 0.06 Ma, the base level fall rate constantly decreased reaching the minimum value of 470 ± 25 m My^{-1}. Then, from 0.54 ± 0.06 Ma to 0.1 ± 0.01 Ma it doubled reaching a value of 1250 ± 100 m My^{-1}, after which it continued to rise again, but less rapidity, achieving the present-day value of 1500 m My^{-1}.

637 6.4 Decomposition of vertical and horizontal ground displacements

638 In order to confirm and quantify the present-day ground displacement rate associated
639 with the residual activity of the Loumar viscous rockslide, satellite SAR Interferometry was
640 applied along the slope and the surrounding areas.

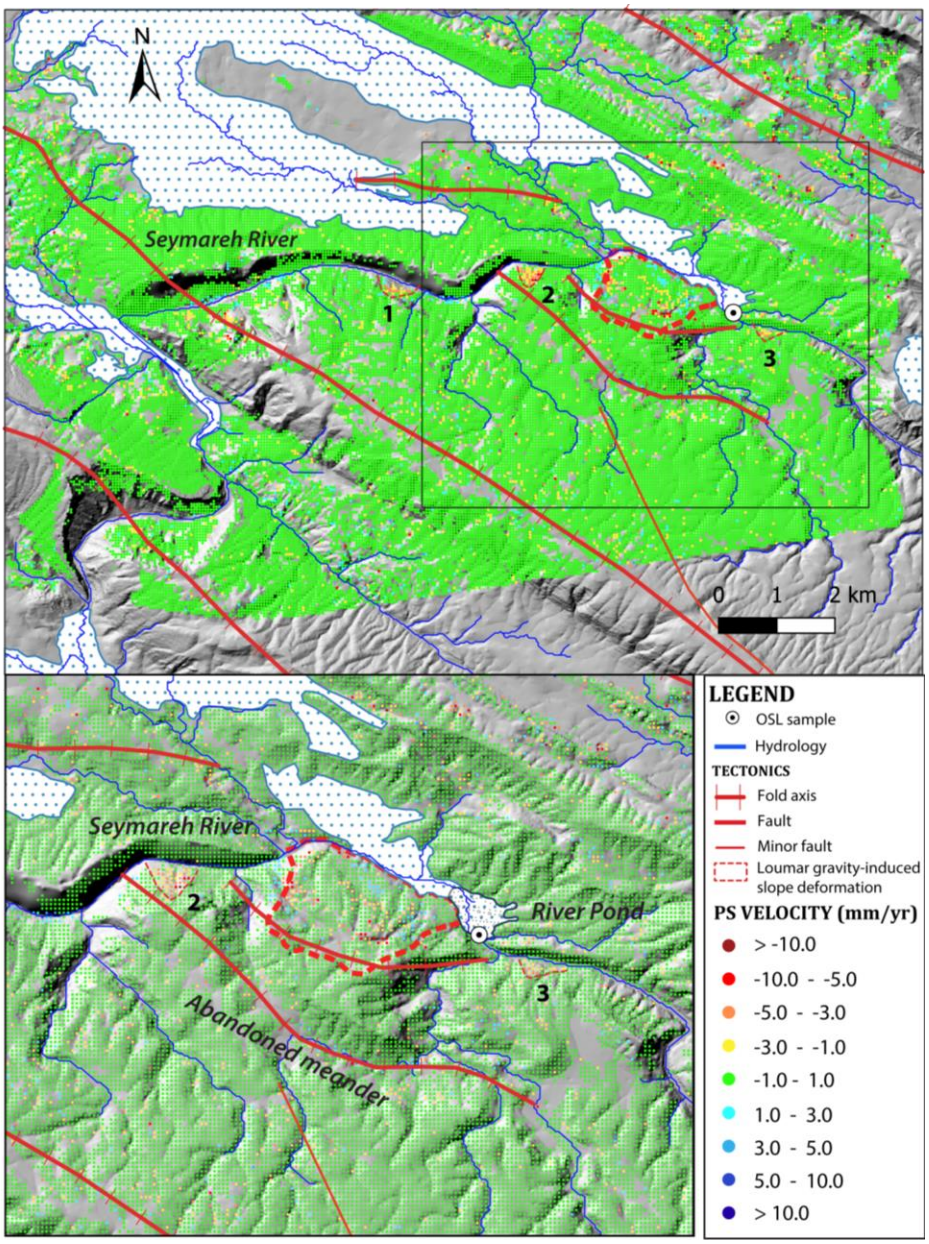

641

642 **Figure 8**. Surface velocity map of the vertical component displacement of the Loumar slope
643 obtained by using a 3D decomposition algorithm developed by NHAZCA Co. Ltd. (**1-3**) Minor
644 shallow landslides emplaced along the Seymareh river gorge.

645 In detail, we performed the decomposition of vertical and horizontal displacements by
646 combining PS InSAR ascending and descending data using proprietary software provided by
647 NHAZCA S.r.l. For the ascending orbit, we analysed 86 Sentinel-1 SAR images in the time

frame between 08 June 2016 and 08 November 2019 while for the descending geometry 95 Sentinel-1 SAR images in the time frame between 16 May 2016 and 21 November 2019.

Figure 8 shows the vertical surface velocity map of the areas, thus allowing to identify different zones showing downward and upward displacements within the Loumar deformation area. As it resulted by the performed analysis, the trenching zone of the gravity-induced slope deformation is affected by the highest negative displacements ranging between -5 and – 7.5 mm y^{-1}, confirming the active tensional release inferred by the remote and field surveys. Regarding the minor scars in the middle of the 25° dipping slope, they show a moderate displacement rate variable between -4 and – 2 mm y^{-1}. Finally, the debris zone where blocks released from the latter zone accumulate, is characterized by a positive displacement rate of about 1 and 3 mm y^{-1}. The above results demonstrate that the rockslide is active and have a progradational style. Moreover, it is important to highlight that in the surrounding areas the highest ground displacement rates are linked to the Seymareh River gorge evolution, allowing to identify at least 3 other minor gravity-induced processes. Such instabilities are shear-driven rockslides that affected the limestone carapace of the Asmari Fm. They are shallow phenomena with short evolution times and displacement rates up to -10 mm y^{-1}.

Despite the difficulty of transposing a decennial observation on an extremely long process, especially if you want to identify the MRC phase in which the process is located, the good fit of the satellite interferometric evidence with the slope landforms testifies an ongoing rock mass creep process.

7 Morpho-evolutionary model

In a tectonically active region slopes composed by contrasting rheological layering, control the evolution of the drainage network as they can release and provide kinematic freedom degrees to deforming rock masses; this results in isolated portion of caprock which starts MRC deformations until slope failure occurs. The results obtained for the Loumar landslide that affects the NE slope of the Gavar anticline in the Simply Folded Zagros, whose evolution is strictly related to the vertical and lateral growth of the anticline and to the evolution of the Seymareh River drainage system, are here discussed.

River rejuvenation due to tectonic uplift was responsible for both the stress and kinematic release of the rock mass which initiated the viscous deformational process until slope failure. we constrained the role of Quaternary tectonics and landscape evolution history of the Gavar fold, as well as the chronology of the events that led to the Loumar gravitational deformation, through remote and field surveys, OSL dating, geomorphometric analysis and river linear inversion modelling. The landscape evolution of the Gavar fold drainage network before and after the slope failure occurrence can be summarized in the following 4 steps and 2 events (Figure 9):

- $\geq$ 1.3±0.1 Ma (Figure 9a) – A main flow direction of the drainage network from NE to SW involved the area, as testified by the wind gaps and the knickpoints cluster at the highest elevation. Then, the Gavar fold started growing and caused a river piracy, deflecting the course towards NW, parallel to the fold structure.
- 1.3±0.1 – 0.46±0.04 Ma (Figure 9b) – The Gavar fold continued to grow up, propagating towards NW so involving the Seymareh River and causing the generation of a meandering gorge. During this phase, the base level fall rate constantly decreased, finally reaching the minimum value of 470 ± 25 m My^{-1}.

- 0.46 ± 0.04 Ma to 0.11 ± 0.01 Ma (Figure 9c) – The base fall rate doubled, reaching a value of 1250 ± 100 m My $^{-1}$ and the folding activity focused on the NE flank of the anticline especially in the corresponding periclinal termination.
- 0.16 ± 0.015 Ma (Figure 9c) – The formation of a parasitic fold, linked to the lateral propagation of the anticline, led to the abandonment of the Seymareh River meander which was located upstream of the deformed slope and to the migration of the river to the present course. This allowed the kinematic release of the NE flank of the Gavar fold, likely starting the MRC deformation process.
- 0.11 ± 0.01 Ma to Present (Figure 9d) – The base-level fall rate continued to rise again, with a lower rate , achieving the present-day value of 1500 m My $^{-1}$. The deformation is localized in the periclinal closure of the fold as demonstrated by the elevation and drop of the younger cluster of knickpoints.
- 5.52±0.36 ka (Figure 9d) – The gravity-induced slope deformation reached the tertiary stage of MRC, evolving to a slope failure with a rock slide mechanism that caused a partial occlusion of the Seymareh River and generated a upstream pond area, characterized by the silty-clay deposits.

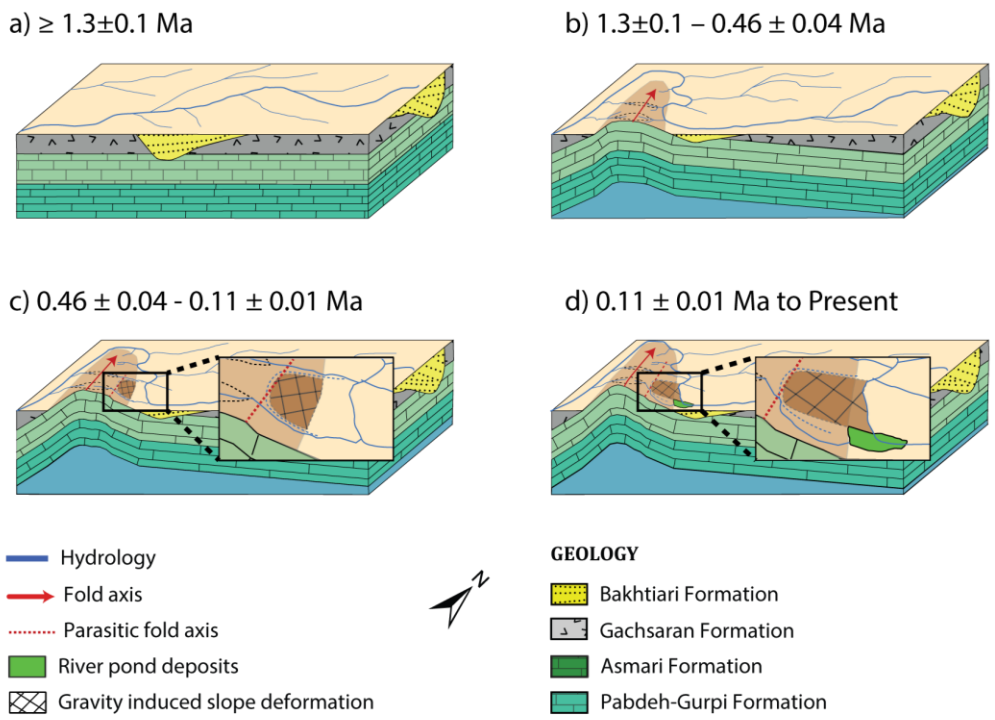

Figure 9. Evolutionary model of the Gavar fold and the Seymareh river valley. See text for explanation.

To date, as resulted by satellite SAR Interferometry, the Loumar rock slide is active with a progradational style and a displacement rate ranging from -5 to -7.5 mm y^{-1} in the upslope trench zone, from -4 to -2 mm y^{-1} in the middle slope zone, and from 1 to 3 mm y^{-1} at the slope toe zone. Moreover, it has been observed that linked to Seymareh River gorge evolution at least 3 other minor ongoing deformations are developing.

8 Conclusion

Transient, tectonically active mountain landscapes are widely affected by landslides in response to gravitational disequilibrium on hillslopes. Mass Rock Creep (MRC) process may become a primary factor for damaging rock masses so leading to slope failures that generate huge rock avalanches. This process acts on a large time-space scale through a continuous and non-linear variation of the stress-strain state of entire portions of slopes, giving rise to processes traditionally known as Deep Seated Gravitational Slope Deformations (DSGSD). In this regard, the limit of theories is represented by the difficulty of precisely and accurately estimating the starting time of the process, of discriminating the distinct phases, as well as determining the viscosity of the rocky matrix. Reconstructing the morpho-evolutionary history of the river valley slope is a key to shed light into the evolution of the gravity-induced deformation as well as into the evaluation of many other interrelated variables. The most important, besides the accurate definition of the geometry and rheological behaviour of the geological formations, are the nonlinearity of the time-displacements relationships as well as the accurate history of the past erosion rate evolution and its nexus with the deforming slope. In this context, a multi-perspective approach that incorporates contributions from linear inversion technique, geomorphometric analysis, remote, and field surveying for OSL dating is presented here. From fluvial networks metrics supported by field and geochronological constraints, we deciphered the main stages of the Gavar fold landscape evolution before and after the slope failure occurrence. From a comparison with Seymareh and Siah-Kuh cases in the Lorestan region, it is possible to observe similar structural and geomorphic predisposing factors for such a kind of gravitational instabilities: 1) constrasting rheological behaviour within the stratigraphy; 2) a moderately dipping downslope (15°-25°); 3) high relief energy; 4) kinematic release, necessary for the initiation of the MRC process. Finally, the estimated starting time for the Loumar case is on the order of 10^2 ka similarly with the Seymareh case study, unlike with Siah-Kuh case in which MRC acted in 10^1 ka. The obtained time constraints will be used as input for the Landscape Evolution Model (LEM) and the stress-strain numerical modeling under creep conditions of the slope to calibrate the rock mass rheology by a back analysis and to discuss the possible role of impulsive triggering (earthquakes) in anticipating the time-to-failure value due to the gravity-driven deformational processes.

Acknowledgments

This research has been supported by the Italian Ministry of the University and Research (no. Grant. B81I17000450001). We are particularly grateful to Reza Nozaem and Mohammad Moumeni Taromsari for his efforts and fruitful scientific contributions to the field work. A special thanks goes to Sean Gallen that allows us to access to his code for linear inversion and to NHAZCA S.r.l., that kindly provided the software for the decomposition of vertical and horizontal displacements.

Data Availability Statement

Vector topographic maps are available on request from the National Cartographic Center of Iran. Satellite images are available online (© Google Earth). Geological maps are available on request from the National Iranian Oil Company. The algorithms for DEM interpolation (ANUDEM) and the codes for the geomorphometric analysis are available, respectively as tool in ArcGIS and as functions in TopoToolbox and TAK (Topographic Analysis Kit). Shapefiles and results of SAR

analysis are stored in this repository: http://doi.org/10.5281/zenodo.4029202. Details on the OSL sampling site and general infos on the deposits are provided in the text of this article. The samples themselves have been obviously distrupted by the analytical procedure.

References

Agard, P., Omrani, J., Jolivet, L., & Mouthereau, F. (2005). Convergence history across Zagros (Iran): constraints from collisional and earlier deformation. *International journal of earth sciences*, *94*(3), 401-419. https://doi.org/10.1007/s00531-005-0481-4

Agliardi, F., Zanchi, A., & Crosta, G. B. (2009). Tectonic vs. gravitational morphostructures in the central Eastern Alps (Italy): constraints on the recent evolution of the mountain range. *Tectonophysics*, *474*(1-2), 250-270. https://doi.org/10.1016/j.tecto.2009.02.019

Alavi, M. (2004). Regional stratigraphy of the Zagros fold-thrust belt of Iran and its proforeland evolution. *American journal of science*, *304*(1), 1-20. https://doi.org/10.2475/ajs.304.1.1

Bert, M. K. (2006). Radar interferometry: Persistent scatterers technique. The Netherlands: Springer.

Boulton, S. J., Stokes, M., & Mather, A. E. (2014). Transient fluvial incision as an indicator of active faulting and Plio-Quaternary uplift of the Moroccan High Atlas. Tectonophysics, 633, 16-33. https://doi.org/10.1016/j.tecto.2014.06.032

Bozzano, F., Martino, S., Montagna, A., & Prestininzi, A. (2012). Back analysis of a rock landslide to infer rheological parameters. *Engineering Geology*, *131*, 45-56. https://doi.org/10.1016/j.enggeo.2012.02.003

Bozzano, F., Della Seta, M., & Martino, S. (2016). Time-dependent evolution of rock slopes by a multi-modelling approach. *Geomorphology*, *263*, 113-131. https://doi.org/10.1016/j.geomorph.2016.03.031

Burbank, D. W., & Anderson, R. S. (2011). *Tectonic geomorphology*. John Wiley & Sons, Ltd., Chichester, West Sussex, UK.

Casciello, E., Vergés, J., Saura, E., Casini, G., Fernández, N., Blanc, E., ... & Hunt, D. W. (2009). Fold patterns and multilayer rheology of the Lurestan Province, Zagros simply folded belt (Iran). *Journal of the Geological Society*, *166*(5), 947-959. https://doi.org/10.1144/0016-76492008-138

Chigira, M. (1992). Long-term gravitational deformation of rocks by mass rock creep. *Engineering Geology*, *32*(3), 157-184. https://doi.org/10.1016/0013-7952(92)90043-X

Chigira, M. (2009). September 2005 rain-induced catastrophic rockslides on slopes affected by deep-seated gravitational deformations, Kyushu, southern Japan. *Engineering Geology*, *108*(1-2), 1-15. https://doi.org/10.1016/j.enggeo.2009.03.005

Clark, M. K., Maheo, G., Saleeby, J., & Farley, K. A. (2005). The non-equilibrium landscape of the southern Sierra Nevada, California. *GsA Today*, *15*(9), 4. https://doi.org/10:1130/1052-5173(2005)0152.0.CO;2

798 Crosby, B. T., & Whipple, K. X. (2006). Knickpoint initiation and distribution within fluvial
799 networks: 236 waterfalls in the Waipaoa River, North Island, New
800 Zealand. *Geomorphology*, *82*(1-2), 16-38.
801 https://doi.org/10.1016/j.geomorph.2005.08.023

802 Crosta, G. B., Frattini, P., & Agliardi, F. (2013). Deep seated gravitational slope deformations in
803 the European Alps. *Tectonophysics*, *605*, 13-33.
804 https://doi.org/10.1016/j.tecto.2013.04.028

805 Delchiaro, M., Della Seta, M., Martino, S., Dehbozorgi, M., & Nozaem, R. (2019).
806 Reconstruction of river valley evolution before and after the emplacement of the giant
807 Seymareh rock avalanche (Zagros Mts., Iran). *Earth Surface Dynamics*, *7*(4), 929-947.
808 https://doi.org/10.5194/esurf-7-929-2019

809 Delchiaro, M., Rouhi, J., Della Seta, M., Martino, S., Nozaem, R., & Dehbozorgi, M. (2020a).
810 The Giant Seymareh Landslide (Zagros Mts., Iran): A Lesson for Evaluating Multi-
811 temporal Hazard Scenarios. In *Applied Geology* (pp. 209-225). Springer, Cham.
812 https://doi.org/10.1007/978-3-030-43953-8_13

813 Delchiaro M, Mele E, Della Seta M, Martino S, Esposito C, Mazzanti P (2020b). Quantitative
814 investigation of a Mass Rock Creep deforming slope through A-Din SAR and
815 geomorphometry. Landslide Full color book (in press).

816 Della Seta, M., Esposito, C., Marmoni, G. M., Martino, S., Mugnozza, G. S., & Troiani, F.
817 (2017). Morpho-structural evolution of the valley-slope systems and related implications
818 on slope-scale gravitational processes: New results from the Mt. Genzana case history
819 (Central Apennines, Italy). *Geomorphology*, *289*, 60-77.
820 https://doi.org/10.1016/j.geomorph.2016.07.003

821 DiBiase, R. A., & Whipple, K. X. (2011). The influence of erosion thresholds and runoff
822 variability on the relationships among topography, climate, and erosion rate. *Journal of*
823 *Geophysical Research: Earth Surface*, *116*(F4). https://doi.org/10.1029/2011JF002095

824 Discenza, M. E., Esposito, C., Martino, S., Petitta, M., Prestininzi, A., & Mugnozza, G. S.
825 (2011). The gravitational slope deformation of Mt. Rocchetta ridge (central Apennines,
826 Italy): geological-evolutionary model and numerical analysis. *Bulletin of Engineering*
827 *Geology and the Environment*, *70*(4), 559-575. https://doi.org/10.1007/s10064-010-0342-
828 7

829 Elyasi, A., Goshtasbi, K., Saeidi, O., & Torabi, S. R. (2014). Stress determination and
830 geomechanical stability analysis of an oil well of Iran. *Sadhana*, *39*(1), 207-220.
831 https://doi.org/10.1007/s12046-013-0224-3

832 Ferretti, A., Prati, C., & Rocca, F. (2000). Nonlinear subsidence rate estimation using permanent
833 scatterers in differential SAR interferometry. *IEEE Transactions on geoscience and*
834 *remote sensing*, *38*(5), 2202-2212. https://doi.org/10.1109/36.868878

835 Ferretti, A., Prati, C., & Rocca, F. (2001). Permanent scatterers in SAR interferometry. *IEEE*
836 *Transactions on geoscience and remote sensing*, *39*(1), 8-20.
837 https://doi.org/10.1109/36.898661

Forte, A. M., & Whipple, K. X. (2019). Short communication: The Topographic Analysis Kit (TAK) for TopoToolbox, *Earth Surface Dynamics*, 7, 87–95. https://doi.org/10.5194/esurf-7-87-2019

Fox, M., Goren, L., May, D. A., & Willett, S. D. (2014). Inversion of fluvial channels for paleorock uplift rates in Taiwan. *Journal of Geophysical Research: Earth Surface*, *119*(9), 1853-1875. https://doi.org/10.1002/2014JF003196

Gallen, S. F. (2018). Lithologic controls on landscape dynamics and aquatic species evolution in post-orogenic mountains. *Earth and Planetary Science Letters*, *493*, 150-160. https://doi.org/10.1016/j.epsl.2018.04.029

Golonka, J. (2004). Plate tectonic evolution of the southern margin of Eurasia in the Mesozoic and Cenozoic. *Tectonophysics*, *381*(1-4), 235-273. https://doi.org/10.1016/j.tecto.2002.06.004

Goren, L., Fox, M., & Willett, S. D. (2014). Tectonics from fluvial topography using formal linear inversion: Theory and applications to the Inyo Mountains, California. *Journal of Geophysical Research: Earth Surface*, *119*(8), 1651-1681. https://doi.org/10.1002/2014JF003079

Hanssen, R. F. (2005). Satellite radar interferometry for deformation monitoring: a priori assessment of feasibility and accuracy. *International journal of applied earth observation and geoinformation*, *6*(3-4), 253-260. https://doi.org/10.1016/j.jag.2004.10.004

Harkins, N., Kirby, E., Heimsath, A., Robinson, R., & Reiser, U. (2007). Transient fluvial incision in the headwaters of the Yellow River, northeastern Tibet, China. *Journal of Geophysical Research: Earth Surface*, *112*(F3). https://doi.org/10.1029/2006JF000570

Hatzfeld, D., Authemayou, C., Van der Beek, P., Bellier, O., Lavé, J., Oveisi, B., Tatar, M., Tavakoli, F., Walpersdorf, A., and Yamini-Fard, F (2010). The kinematics of the Zagros mountains (Iran). *Geological Society, London, Special Publications*, *330*(1), 19-42. https://doi.org/10.1144/SP330.3

Homke, S., Vergés, J., Garcés, M., Emami, H., & Karpuz, R. (2004). Magnetostratigraphy of Miocene–Pliocene Zagros foreland deposits in the front of the Push-e Kush arc (Lurestan Province, Iran). *Earth and Planetary Science Letters*, *225*(3-4), 397-410. https://doi.org/10.1016/j.epsl.2004.07.002

Howard, A. D., & Kerby, G. (1983). Channel changes in badlands. *Geological Society of America Bulletin*, *94*(6), 739-752. https://doi.org/10.1130/0016-7606(1983)94<739:CCIB>2.0.CO;2

Hutchinson, M., Xu, T., & Stein, J. (2011). Recent Progress in the ANUDEM Elevation Gridding Procedure. *Geomorphometry*, 19–22. https://doi.org/10.1002/osp4.29

James, G. A., & Wynd, J. G. (1965). Stratigraphic nomenclature of Iranian oil consortium agreement area. *AAPG bulletin*, *49*(12), 2182-2245. https://doi.org/10.1306/A663388A-16C0-11D7-8645000102C1865D

Larsen, I. J., & Montgomery, D. R. (2012). Landslide erosion coupled to tectonics and river incision. *Nature Geoscience*, *5*(7), 468-473. https://doi.org/10.1038/ngeo1479

878 Llewellyn, P. G. (1974). Palganeh. 1:100 000 Geological Map. *Iran Oil Operating Companies, Geological Exploration Division, Tehran, Iran*

880 Kirby, E., & Whipple, K. X. (2012). Expression of active tectonics in erosional landscapes. *Journal of Structural Geology*, *44*, 54-75. https://doi.org/10.1016/j.jsg.2012.07.009

883 Korup, O., & Schlunegger, F. (2007). Bedrock landsliding, river incision, and transience of geomorphic hillslope-channel coupling: Evidence from inner gorges in the Swiss Alps. *Journal of Geophysical Research: Earth Surface*, *112*(F3). https://doi.org/10.1029/2006JF000710

887 Korup, O., Clague, J. J., Hermanns, R. L., Hewitt, K., Strom, A. L., & Weidinger, J. T. (2007). Giant landslides, topography, and erosion. *Earth and Planetary Science Letters*, *261*(3-4), 578-589. https://doi.org/10.1016/j.epsl.2007.07.025

890 Korup, O., Densmore, A. L., & Schlunegger, F. (2010). The role of landslides in mountain range evolution. *Geomorphology*, *120*(1-2), 77-90. https://doi.org/10.1016/j.geomorph.2009.09.017

893 Ma, Z., Zhang, H., Wang, Y., Tao, Y., & Li, X. (2020). Inversion of Dadu River Bedrock Channels for the Late Cenozoic Uplift History of the Eastern Tibetan Plateau. *Geophysical Research Letters*, *47*(4), e2019GL086882. https://doi.org/10.1029/2019GL086882

897 Martino, S., Prestininzi, A., & Mugnozza, G. S. (2004). Geological-evolutionary model of a gravity-induced slope deformation in the carbonate Central Apennines (Italy). *Quarterly journal of engineering geology and hydrogeology*, *37*(1), 31-47. https://doi.org/10.1144/1470-9236/03-030

901 Martino, S., Della Seta, M., & Esposito, C. (2017). Back-analysis of rock landslides to infer rheological parameters. *Rock Mechanics and Engineering*, *3*, 237-269.

903 McQuarrie, N. (2004). Crustal scale geometry of the Zagros fold–thrust belt, Iran. *Journal of Structural Geology*, *26*(3), 519-535. https://doi.org/10.1016/j.jsg.2003.08.009

905 Montgomery, D. R., & Brandon, M. T. (2002). Topographic controls on erosion rates in tectonically active mountain ranges. *Earth and Planetary Science Letters*, *201*(3-4), 481-489. https://doi.org/10.1016/S0012-821X(02)00725-2

908 Mouthereau, F., Lacombe, O., & Vergés, J. (2012). Building the Zagros collisional orogen: timing, strain distribution and the dynamics of Arabia/Eurasia plate convergence. *Tectonophysics*, *532*, 27-60. https://doi.org/10.1016/j.tecto.2012.01.022

911 Murray, A. S., & Olley, J. M. (2002). Precision and accuracy in the optically stimulated luminescence dating of sedimentary quartz: a status review. *Geochronometria*, *21*(1), 1-16.

914 Oberlander, T. M. (1965). The Zagros streams: a new interpretation of transverse drainage in an orogenic zone. *Syracuse Geographical Series*.

916 Oberlander, T. M. (1968). The origin of the Zagros defiles. *The Cambridge History of Iran*, *1*, 195-211.

Oberlander, T. M. (1985). Origin of drainage transverse to structures in orogens. In *Tectonic geomorphology* (Vol. 15, pp. 155-182). Allen and Unwin Boston.

Pánek, T., & Klimeš, J. (2016). Temporal behavior of deep-seated gravitational slope deformations: A review. *Earth-Science Reviews, 156*, 14-38. https://doi.org/10.1016/j.earscirev.2016.02.007

Paul, A., Hatzfeld, D., Kaviani, A., Tatar, M., & Péquegnat, C. (2010). Seismic imaging of the lithospheric structure of the Zagros mountain belt (Iran). *Geological Society, London, Special Publications, 330*(1), 5-18. https://doi.org/10.1144/SP330.2

Perron, J. T., & Royden, L. (2013). An integral approach to bedrock river profile analysis. *Earth Surface Processes and Landforms, 38*(6), 570-576. https://doi.org/10.1002/esp.3302

Petley, D. N., & Allison, R. J. (1997). The mechanics of deep-seated landslides. *Earth Surface Processes and Landforms: The Journal of the British Geomorphological Group, 22*(8), 747-758. https://doi.org/10.1002/(SICI)1096-9837(199708)22:8<747::AID-ESP767>3.0.CO;2-%23

Pritchard, D., Roberts, G. G., White, N. J., & Richardson, C. N. (2009). Uplift histories from river profiles. *Geophysical Research Letters, 36*(24). https://doi.org/10.1029/2009GL040928

Rajabi, A. M., Mahdavifar, M. R., Khamehchiyan, M., & Del Gaudio, V. (2011). A new empirical estimator of coseismic landslide displacement for Zagros Mountain region (Iran). *Natural Hazards, 59*(2), 1189-1203. https://doi.org/10.1007/s11069-011-9829-1

Ramsey, L. A., Walker, R. T., & Jackson, J. (2008). Fold evolution and drainage development in the Zagros mountains of Fars province, SE Iran. *Basin Research, 20*(1), 23-48. https://doi.org/10.1111/j.1365-2117.2007.00342.x

Roberts, G. G., & White, N. (2010). Estimating uplift rate histories from river profiles using African examples. *Journal of Geophysical Research: Solid Earth, 115*(B2). https://doi.org/10.1029/2009JB006692

Roering, J. J., Perron, J. T., & Kirchner, J. W. (2007). Functional relationships between denudation and hillslope form and relief. *Earth and Planetary Science Letters, 264*(1-2), 245-258. https://doi.org/10.1016/j.epsl.2007.09.035

Royden, L., & Taylor Perron, J. (2013). Solutions of the stream power equation and application to the evolution of river longitudinal profiles. *Journal of Geophysical Research: Earth Surface, 118*(2), 497-518. https://doi.org/10.1002/jgrf.20031

Rudge, J. F., Roberts, G. G., White, N. J., & Richardson, C. N. (2015). Uplift histories of Africa and Australia from linear inverse modeling of drainage inventories. *Journal of Geophysical Research: Earth Surface, 120*(5), 894-914. https://doi.org/10.1002/2014JF003297

Saito, M. (1969, August). Forecasting time of slope failure by tertiary creep. In *Proc. 7th Int. Conf on Soil Mechanics and Foundation Engineering, Mexico City* (Vol. 2, pp. 677-683).

Schmidt, J. L., Zeitler, P. K., Pazzaglia, F. J., Tremblay, M. M., Shuster, D. L., & Fox, M. (2015). Knickpoint evolution on the Yarlung river: Evidence for late Cenozoic uplift of

the southeastern Tibetan plateau margin. *Earth and Planetary Science Letters*, *430*, 448-457. https://doi.org/10.1016/j.epsl.2015.08.041

Schwanghart, W., & Scherler, D. (2014). TopoToolbox 2–MATLAB-based software for topographic analysis and modeling in Earth surface sciences. *Earth Surface Dynamics*, *2*(1), 1-7. https://doi.org/10.5194/esurf-2-1-2014

Shafiei, A., & Dusseault, M. B. (2008, January). Geomechanical properties of a conglomerate from Iran. In *The 42nd US Rock Mechanics Symposium (USRMS)*. American Rock Mechanics Association. https://doi.org/10.13140/RG.2.1.1722.7684

Stampfli, G. M., & Borel, G. D. (2002). A plate tectonic model for the Paleozoic and Mesozoic constrained by dynamic plate boundaries and restored synthetic oceanic isochrons. *Earth and Planetary Science Letters*, *196*(1-2), 17-33. https://doi.org/10.1016/S0012-821X(01)00588-X

Talbot, C. J., & Alavi, M. (1996). The past of a future syntaxis across the Zagros. *Geological Society, London, Special Publications*, *100*(1), 89-109. https://doi.org/10.1144/GSL.SP.1996.100.01.08

Tozer, R. S., Hertle, M., Petersen, H. I., & Zinck-Jørgensen, K. (2019). Quantifying vertical movements in fold and thrust belts: subsidence, uplift and erosion in Kurdistan, northern Iraq. *Geological Society, London, Special Publications*, *490*, SP490-2019. https://doi.org/10.1144/SP490-2019-118

Tsou, C. Y., Chigira, M., Matsushi, Y., & Chen, S. C. (2014). Fluvial incision history that controlled the distribution of landslides in the Central Range of Taiwan. *Geomorphology*, *226*, 175-192. doi: 10.1016/j.geomorph.2014.08.015

Tucker, G. E., & Slingerland, R. (1996). Predicting sediment flux from fold and thrust belts. *Basin research*, *8*(3), 329-349. https://doi.org/10.1046/j.1365-2117.1996.00238.x

Tucker, G. E., & Whipple, K. X. (2002). Topographic outcomes predicted by stream erosion models: Sensitivity analysis and intermodel comparison. *Journal of Geophysical Research: Solid Earth*, *107*(B9), ETG-1. https://doi.org/10.1029/2001JB000162

Vergés, J., Goodarzi, M. G. H., Emami, H., Karpuz, R., Efstathiou, J., & Gillespie, P. (2011). Multiple detachment folding in Pusht-e Kuh arc, Zagros: Role of mechanical stratigraphy. https://doi.org/10.1306/13251333M942899

Vergés, J., Emami, H., Garcés, M., Beamud, E., Homke, S., & Skott, P. (2019). Zagros foreland fold belt timing across Lurestan to constrain Arabia–Iran collision. In *Developments in structural geology and tectonics* (Vol. 3, pp. 29-52). Elsevier. https://doi.org/10.1016/B978-0-12-815048-1.00003-2

Walsh, L. S., Martin, A. J., Ojha, T. P., & Fedenczuk, T. (2012). Correlations of fluvial knickzones with landslide dams, lithologic contacts, and faults in the southwestern Annapurna Range, central Nepalese Himalaya. *Journal of Geophysical Research: Earth Surface*, *117*(F1). https://doi.org/10.1029/2011JF001984

Whipple, K. X., & Tucker, G. E. (1999). Dynamics of the stream-power river incision model: Implications for height limits of mountain ranges, landscape response timescales, and

research needs. *Journal of Geophysical Research: Solid Earth*, *104*(B8), 17661-17674. https://doi.org/10.1029/1999JB900120

Wilson, J. P., & Gallant, J. C. (Eds.). (2000). *Terrain analysis: principles and applications*. John Wiley & Sons.

Wintle, A. G., & Murray, A. S. (2006). A review of quartz optically stimulated luminescence characteristics and their relevance in single-aliquot regeneration dating protocols. *Radiation measurements*, *41*(4), 369-391. https://doi.org/10.1016/j.radmeas.2005.11.001

Wobus, C., Whipple, K. X., Kirby, E., Snyder, N., Johnson, J., Spyropolou, K., Crosby, B. T. & Sheehan, D. (2006). Tectonics from topography: Procedures, promise, and pitfalls. *Special papers-geological society of america*, *398*, 55.

Yamato, P., Kaus, B. J., Mouthereau, F., & Castelltort, S. (2011). Dynamic constraints on the crustal-scale rheology of the Zagros fold belt, Iran. *Geology*, *39*(9), 815-818. https://doi.org/10.1130/G32136.1

Zebari, M., Grützner, C., Navabpour, P., & Ustaszewski, K. (2019). Relative timing of uplift along the Zagros Mountain Front Flexure (Kurdistan Region of Iraq): Constrained by geomorphic indices and landscape evolution modeling. *Solid Earth*, *10*(3), 663-682. https://doi.org/10.5194/se-10-663-2019